HHS Public Access

Author manuscript

Immunity. Author manuscript; available in PMC 2022 October 12.

Published in final edited form as:

Immunity. 2021 October 12; 54(10): 2321–2337.e10. doi:10.1016/j.immuni.2021.09.001.

Disruption of the endopeptidase ADAM10-Notch signaling axis leads to skin dysbiosis and innate lymphoid cell-mediated hair follicle destruction

Keiko Sakamoto[1], **Seon-Pil Jin**[1], **Shubham Goel**[1], **Jay-Hyun Jo**[2], **Benjamin Voisin**[1,5], **Doyoung Kim**[1,6], **Vinod Nadella**[1], **Hai Liang**[2], **Tetsuro Kobayashi**[1,7], **Xin Huang**[3], **Clay Deming**[3], **Keisuke Horiuchi**[4], **Julia A. Segre**[3], **Heidi H. Kong**[2], **Keisuke Nagao**[1,8,*]

[1]Cutaneous Leukocyte Biology Section, Dermatology Branch, National Institute of Arthritis and Musculoskeletal and Skin Diseases, National Institutes of Health, Bethesda, MD 20892, USA

[2]Cutaneous Microbiome and Inflammation Section, Dermatology Branch, National Institute of Arthritis and Musculoskeletal and Skin Diseases, National Institutes of Health, Bethesda, MD 20892, USA

[3]Microbial Genomics Section, Translational and Functional Genomics Branch, National Human Genome Research Institute, National Institutes of Health, Bethesda, MD 20892, USA

[4]Department of Orthopedic Surgery, National Defense Medical College, Saitama 359-8513, Japan

[5]Current affiliation: CNRS UPR 3572, IBMC, University of Strasbourg, 67000 Strasbourg, France

[6]Current affiliation: Department of Dermatology and Cutaneous Biology Research Institute, Yonsei University College of Medicine, Seoul, South Korea

[7]Current affiliation: Laboratory for Innate Immune Systems, RIKEN Center for Integrative Medical Sciences, Yokohama, Japan

[8]Lead contact

Summary

Hair follicles (HF) function as hubs for stem cells, immune cells, and commensal microbes, which must be tightly regulated during homeostasis and transient inflammation. Here, we found that transmembrane endopeptidase ADAM10 expression in upper HFs was crucial for regulating

*Corresponding author: Keisuke Nagao, M.D., Ph.D., Cutaneous Leukocyte Biology Section, Dermatology Branch, NIAMS, NIH, keisuke.nagao@nih.gov.

Author contributions: K.S. and K.N. designed the experiments and overall study. K.S. and K.N. wrote the manuscript. K.S. performed majority of the *in vitro* and *in vivo* experiments. SP.J., B.V., and DY.K. performed transcriptome analysis. H.L and T.K. assisted experiments. V.N. and S.G. performed Western blot analysis. JH.J., X.H., C.D., H.H.K., and J.A.S. performed microbiome analysis. K.H. provided *Adam*$10^{f/f}$ mice and intellectual input. All authors discussed the results and participated in the manuscript preparation and editing.

Declaration of interests: Authors declare no competing interests.

skin microbiota and protecting HFs and their stem cell niche from inflammatory destruction. Ablation of the ADAM10-Notch signaling axis impaired innate epithelial barrier and enabled *Corynebacterium* species to predominate the microbiome. Dysbiosis triggered group 2 innate lymphoid cells-mediated inflammation in an IL-7 receptor-, S1P receptor 1- and CCR6-dependent manner, leading to pyroptotic cell death of HFs and irreversible alopecia. Double-stranded RNA-induced ablation models indicated that ADAM10-Notch signaling axis bolsters epithelial innate immunity by promoting β-defensin-6 expression downstream of type I interferon responses. Thus, ADAM10-Notch signaling axis-mediated regulation of host-microbial symbiosis crucially protects HFs from inflammatory destruction, which has implications for strategies to sustain tissue integrity during chronic inflammation.

Graphical Abstract

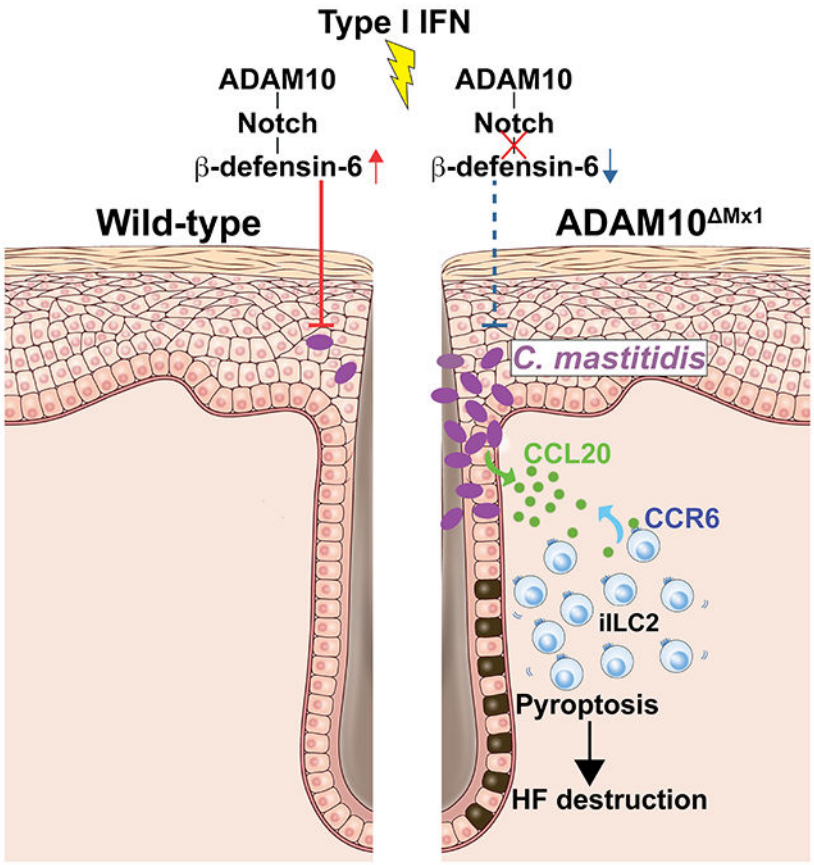

eTOC

Host symbiosis with commensal microorganisms must be maintained during homeostasis and inflammation. Sakamoto et al show that the innate epithelial barrier bolstered by ADAM10-Notch signaling in type I interferon-responsive upper hair follicles was crucial for regulating the follicular microbiome, inhibition of which led to downregulation of β-defensin-6, dysbiosis and inflammatory destruction of the hair follicles mediated by innate lymphoid cells.

Keywords

alopecia; hair follicles; innate lymphoid cells; skin microbiota; ADAM10; Notch; dysbiosis; pyroptosis

Introduction

Hair follicles (HFs) are crucial structures in the mammalian skin. Owing to the stem cells in the bulge area, HFs self-renew during homeostasis and upon skin injury (Cotsarelis et al., 1990; Gonzales and Fuchs, 2017), producing hair shafts, which provide the first line of physical defense. HFs are immunologically active, particularly in the upper HFs (uHFs) which consist of the infundibulum (follicular opening), and isthmus (narrowed area of the HFs above the bulge). Upon sensing mechanical stress, uHFs produce the chemokines, CCL2 and CCL20, that recruit dendritic cells to sites of minor trauma via their respective receptors, CCR2 and CCR6 (Nagao et al., 2012). Resident memory T cells are folliculotropic and rely on uHF-derived cytokines interleukin (IL)-7 and IL-15 for their survival in skin (Adachi et al., 2015). Epidermal innate lymphoid cells (ILCs) also localize to the uHFs guided by CCR6, where they gain access to the cytokines thymic stromal lymphopoietin and IL-7 that they critically depend on (Kobayashi et al., 2019). These findings highlight HFs as regulators of skin immunity that govern the positioning and tissue-residency of immune cells.

Dysregulated inflammation can lead to hair loss disorders in humans. In alopecia areata, infiltration of $CD8^+$ T cells around the anagen (growth phase) portion of the HFs triggers the hair cycles to prematurely enter catagen (regression phase) resulting in hair loss, which is reversible in nature. Primary cicatricial alopecia (PCA) consist of several subsets that can be categorized into lymphocytic and neutrophilic subsets. Lymphocytic subtypes include frontal fibrosing alopecia, lichen planopilaris and central centrifugal cicatricial alopecia (CCCA) (Harries and Paus, 2010). In contrast to alopecia areata, $CD8^+$ T cells in the two former and $CD4^+$ T cells in the latter infiltrate the bulge area of HFs, leading to the destruction of the stem cell niche, further resulting in irreversible alopecia (Anzai et al., 2019; Flamm et al., 2020). While T cell involvement in pathophysiology of alopecia seems evident, whether ILCs can contribute to inflammatory destruction of HFs remains unexplored.

The invaginations of HFs serve as niches for commensal microbes (Belkaid and Segre, 2014). Commensal microbes provide stimuli that maintain effective immunity as well as tissue repair (Di Domizio et al., 2020; Harrison et al., 2019; Linehan et al., 2018; Naik et al., 2015). Epidermal ILCs produce TNF and lymphotoxin receptor ligands and regulate the secretion of antimicrobial free fatty acids by the sebaceous glands, thereby tuning the balance of skin microbiota (Kobayashi et al., 2019). Thus, the bilateral communications between the host and its microbiota are integral to the structural, immunological, and microbial homeostasis in the skin. These multifaceted aspects of HFs highlight them as interactive hubs for stem cells, host immunity, and the microbiota, providing an attractive model in which mechanisms of host-microbial symbiosis may be studied.

A disintegrin and metalloproteinase (ADAM) is a large family of transmembrane endopeptidases that regulate various biological processes through ectodomain shedding of a broad spectrum of substrates (Edwards et al., 2008). A prototypic function of ADAMs is exemplified by ADAM17 that cleaves membrane-bound forms of TNF and epidermal growth factor receptor ligands to release active forms that regulate immunity and cell proliferation (Edwards et al., 2008). We previously reported that ablation of ADAM17 from epidermal keratinocytes leads to skin dysbiosis that drives eczematous skin inflammation, highlighting an ADAM family member as a regulator of bacterial colonization on the skin surface through mediating epidermal growth factor receptor signaling (Kobayashi et al., 2015). The genomic deletion of ADAM10, another extensively studied member of ADAMs, is embryonic lethal (Hartmann et al., 2002). A crucial role of ADAM10 during HF morphogenesis has been demonstrated by tissue-specific ablation from the developing epidermis via mediation of Notch signaling (Weber et al., 2011). Sequential cleavage of Notch by ADAM10 and γ–secreatase releases the Notch intracellular domain (NICD). NICD translocates to the nucleus to promote gene transcription in cooperation with the DNA-binding protein, RBPJ and the co-activator Mastermind. ADAM10 also serves as a receptor for a bacterial toxin (Wilke and Bubeck Wardenburg, 2010). Given these functions regarding tissue homeostasis and antimicrobial responses, we hypothesized that ADAM10 might play crucial roles in facilitating host-microbial symbiosis that enable HFs to function as hubs for host immunity and the microbiota.

Maintenance of tissue homeostasis and function is crucial during transient inflammatory responses. Systemic cues, such as type I interferons (IFN), that are produced in response to viral infections is thought to trigger not only alopecia but also autoimmune diseases such as myositis, lupus erythematosus and type I diabetes mellitus (Adler and Christopher-Stine, 2018; Filippi and von Herrath, 2008; Illescas-Montes et al., 2019; Ito and Tokura, 2012; Rodriguez and Duvic, 2008). Thus, viral infections, through their activation of host immunity and other mechanisms, may serve as a second hit that contribute to autoimmune disease onset. Moreover, bacterial infections commonly arise secondarily to viral infections (Manohar et al., 2020), reiterating that exuberant immunological cues elicited by viruses could confound tissue function and impair host-defense mechanisms against bacteria.

Herein, we show that type I IFN-responsive uHF cells utilized the ADAM10-Notch signaling axis to regulate the follicular microbiome via mouse β-defensin-6 (mBD-6). In the absence of ADAM10-Notch signalin axis, the follicular microbiome was predominated by *Corynebacterium mastitidis*, which triggered ILC2-mediated inflammation, leading to pyroptotic cell death and irreversible alopecia.

RESULTS

Induced ablation of ADAM10 in type I IFN-responsive HF cells results in inflammatory transcriptome

Given that uHFs are immunologically active and anatomically accessible to commensal bacteria, we hypothesized that mechanisms related to host-microbial symbiosis are crucial in this compartment. First, to precisely identify HF keratinocyte subsets via flow cytometry, we refined our previous approach (Nagao et al., 2012) by incorporating the HF marker, CD200

(Rosenblum et al., 2004). EpCAM was expressed by all keratinocytes, whereas CD200 expression was restricted to the HFs (Fig. 1A and 1B). The bulge area was identified as $CD200^{+}CD34^{+}$ cells, and $CD200^{+}CD34^{-}$ uHFs were further divided into $EpCAM^{+}Sca1^{-}$ isthmus and $EpCAM^{+}Sca1^{+}$ infundibulum.

Next, we explored if uHFs were responsive to systemic type I IFN. We used *Mx1*-Cre mice, in which the expression of Cre recombinase is driven by the promoter of the type I IFN-responsive gene, *Mx1* (Dickensheets et al., 2013; Kühn et al., 1995). Cre activation is obtained by intraperitoneal injection of poly (I:C), thereby representing a model of experimental anti-viral immunity. *Mx1*-Cre mice were crossed with ROSA26-eYFP ($ROSA26YFP^{\Delta Mx1}$) mice to enable the detection of IFN-responsive cells via yellow fluorescent protein (YFP) expression. Flow cytometry analysis in $ROSA26YFP^{\Delta Mx1}$ mice that were injected with the poly(I:C) revealed YFP induction in 20–30% of uHFs, but not in the bulge cells (Fig. 1C), indicating that HF subsets exhibited differential reactivity to type I IFN and that *Mx1*-Cre mice could be utilized to target immunologically active uHFs.

$ROSA26YFP^{\Delta Mx1}$ mice were further crossed with $Adam10^{f/f}$ mice ($ADAM10;ROSA26YFP^{\Delta Mx1}$) to simultaneously ablate ADAM10 in cells marked as YFP-positive. Four days after poly(I:C) injection, YFP^{+} uHF cells were sorted for RNA sequencing (RNA-seq). Analysis of differentially expressed genes (DEG) revealed effective *Adam10* ablation from the uHFs but not from the bulge cells (Fig. 1D). ADAM10 ablation led to broad transcriptomic changes in the uHFs (Table S1, Fig. 1E). Pathway enrichment analysis of DEGs revealed marked upregulation of immunological pathways driven by genes encoding chemokines and cytokines (e.g., *Ccl2*, *Ccl20*, *Il1a*), and those associated with antigen presentation via MHC II (e.g., *Cd74*, *Ciita*, *H2-ab1*) (Fig. 1E, 1F, Table S1). Upregulation of genes related to programmed cell death pathway was also noted (e.g., *Casp4*). Downregulated pathways included those related to structural homeostasis, such as Notch signaling (e.g., *Notch1*), Wnt signaling (e.g., *Wnt5b*), and cell adhesion (e.g., *Itgb5*, *Col1a2*) pathways.

Despite their unaltered *Adam10* expression (Fig. 1D), bulge cells also displayed broad transcriptomic changes (Fig. 1G, 1H, Table S2). Pathway enrichment analysis revealed upregulation of pathways including those pertaining to inflammation that were driven by genes encoding chemokines and cytokines (e.g., *Ccl20*, *Il1b*) and those related to programmed cell death (e.g., *Casp1*). Downregulated pathways included positive regulation of Wnt signaling (e.g., *Wnt5*, *Gli1*) and cell adhesion (e.g., *Nrcam*). These findings suggested that the changes triggered in the uHFs upon ADAM10 ablation influenced the bulge to undergo transcriptomic shifts that alluded to altered functions and disrupted immunological quiescence.

Thus, *Adam10* ablation in type I IFN-responsive cells led to transcriptomic alterations with prominent inflammatory profiles not only in the uHFs but also in the bulge, consistent with our hypothesis that ADAM10 expressed by the uHFs was involved in facilitating immunological homeostasis of the entire HF unit.

ADAM10 ablation from uHF cells leads to inflammatory alopecia

While spontaneous phenotypes were unobserved in *Mx1*-Cre x *Adam10*$^{f/f}$ (ADAM10$^{\Delta Mx1}$) mice, long-term observation after poly(I:C) injection revealed the development of progressive alopecia beginning approximately 20 days post-induction, which occurred diffusely at multiple body sites but was most predictable in the chest area with patchiness that enabled reliable quantification (Fig. S1A, Fig. 2A). The areas of alopecia displayed no obvious underlying dermatitis. ADAM10$^{\Delta Mx1}$ mice also displayed reduced hair pigment. Histological analysis revealed lymphocytic infiltration in HFs at day 10 that preceded alopecia onset, which increased thereafter, followed by morphological alteration of HFs (Fig. 2B).

Mx1 promoter is also active in immune cells. Evaluation of type I IFN-responsive cell types in ROSA26YFP$^{\Delta Mx1}$ mice revealed that the vast majority of YFP^{+} cells to be keratinocytes, with a minor population of CD45^{+} immune cells, most of which were CD11b^{+} myeloid cells (Fig. S1B). To first evaluate whether or not the ablation of *Adam10* from immune cells drove the alopecia phenotype, we generated bone marrow (BM) chimeric mice. Lethally-irradiated *Adam10*$^{f/f}$ (WT) mice reconstituted with ADAM10$^{\Delta Mx1}$ BM did not exhibit the alopecia phenotype, whereas the phenotype of ADAM10$^{\Delta Mx1}$ mice reconstituted with WT BM was unrescued (Fig. S1C). To further exclude the roles of myeloid cells, some of which may not be replaced in the transplant setting (Barreiro et al., 2016; Merad et al., 2002), we generated *Csf1r*-Cre x *Adam10*$^{f/f}$ mice to ablate *Adam10* from the broad myeloid cell subsets (Loschko et al., 2016). These mice did not develop alopecia with or without poly(I:C) injection (Fig. S1D). Adoptive transfer of poly(I:C)-induced ADAM10$^{\Delta Mx1}$ lymph node cells into *Rag2*$^{-/-}$ mice led to the reconstitution of T cells (Adachi et al., 2015), but it did not trigger alopecia (Fig. S1E, S1F). Adoptive transfer of poly(I:C)-induced ADAM10$^{\Delta Mx1}$ bone marrow cells into *Rag2*$^{-/-}$*Il2rg*$^{-/-}$ mice primarily led to the reconstitution of ILCs, but this also did not trigger alopecia (Fig. S1E, S1F). Taken together, these data suggested that loss of ADAM10 in keratinocytes, rather than immune cells, was responsible for the alopecia phenotype. To further ascertain that the ablation of *Adam10* from HF compartments caused the alopecia phenotype, we generated reporter mice by crossing ROSA26-eYFP mice with *Lrig1*-Cre^{ERT2} and *Krt15*-Cre^{PGR} mice (Morris et al., 2004; Veniaminova et al., 2013). *Lrig1*-Cre promoter was active only in the uHFs with both standard- and low-dose tamoxifen injection protocols (Zhao et al., 2020), whereas the *Krt15*-Cre promoter was active specifically in the bulge area upon the administration of the progesterone receptor analogue, RU486 (Fig. S1G). Hence, we generated *Lrig1*-Cre^{ERT2} x *Adam10*$^{f/f}$ (ADAM10$^{\Delta Lrig1}$) and *Krt15*-Cre^{PGR} x *Adam10*$^{f/f}$ mice (ADAM10$^{\Delta K15}$), enabling the ablation of *Adam10* specifically from the uHFs and the bulge areas, respectively. Unexpectedly, standard-dose tamoxifen administered to ADAM10$^{\Delta Lrig1}$ mice had a lethal outcome. When ADAM10$^{\Delta Lrig1}$ mice were treated with low-dose tamoxifen, they developed alopecia with HF inflammation that recapitulated ADAM10$^{\Delta Mx1}$ mice (Fig. S1H). ADAM10$^{\Delta K15}$ mice also developed an alopecia phenotype, but unlike ADAM10$^{\Delta Mx1}$ or ADAM10$^{\Delta Lrig1}$ mice, the alopecia was widespread throughout their body surfaces and histological examination revealed cyst formation as the prominent feature (Fig. S1I), suggesting that ablation of *Adam10* from the bulge predominantly

affected structural integrity. Thus, ablation of *Adam10* from the uHFs, which encompassed type I IFN-responsive subsets, led to the inflammatory destruction of HFs.

Inflammatory ILC2s (iILC2s) mediated destruction of HFs

Immunofluorescence microscopy of skin sections from ADAM10$^{\Delta Mx1}$ mice validated follicular accumulation of immune cells (Fig. S2A). Flow cytometry analysis revealed a predominance of Thy1^{+} lymphoid cells and time-course analyses revealed CD4^{+} T cells and Iineage^{-}Thy1^{+} ILCs to be the only immune cell subsets that expanded prior to alopecia onset (Fig. S2B, S2C, Fig. 2C). Thus, to understand which lymphoid cells were involved, we crossed ADAM10$^{\Delta Mx1}$ mice with lymphopenic *Rag2*$^{-/-}$ mice or with *Il7ra*$^{-/-}$ mice, the latter lacking the majority of T cells, ILC2s, and ILC3s (Peschon et al., 1994; Sheikh and Abraham, 2019). While ADAM10$^{\Delta Mx1}$ mice in the *Rag2*$^{-/-}$ background displayed alopecia, those in the *Il7ra*$^{-/-}$ background had an attenuated phenotype (Fig. 2D), suggesting that ILCs, but not T cells, mediated HF inflammation. Unexpectedly, repeated local injections of an anti-Thy1.2 antibody in ADAM10$^{\Delta Mx1}$ *Rag2*$^{-/-}$ mice failed to deplete ILCs and had no impact on the alopecia phenotype (Fig. S2D, S2E).

We therefore sorted CD45^{+} cells from ADAM10$^{\Delta Mx1}$ *Rag2*$^{-/-}$ mouse skin and performed single-cell RNA-seq (scRNA-seq) to characterize ILCs. Unsupervised clustering analysis revealed three major clusters, each identified as a mixture of *Thy1*$^{+}$*CD3e*$^{-}$*Gata3*^{high}*Il1rl1*$^{+}$ ILC2s and *Gata3*^{mid}*Rorc*$^{+}$ ILC3s, *Thy1*$^{+}$*Cd3e*$^{-}$*Cd2*$^{+}$*Gzmc*$^{+}$ cells, likely representing natural killer (NK) cells and/or ILC1s, and *Thy1*$^{-}$*H2-Aa*$^{+}$*Itgam*$^{+}$ myeloid cells (Fig. S2F, S2G, Table S3). The chemokine receptor gene *Ccr2* was differentially expressed by NK cell-ILC1 cluster and myeloid cell cluster, whereas *Ccr6* was specifically expressed by the ILC2-ILC3 cluster (Fig. S2G). Analysis of ILCs in *Rag2*-sufficient ADAM10$^{\Delta Mx1}$ mice validated CCR6 expression on most ILCs (Fig. 2E). While CCR6 expression has been linked to subsets of ILC3s (Melo-Gonzalez and Hepworth, 2017), the vast majority of ILCs in ADAM10$^{\Delta Mx1}$ mice were GATA3^{high} cells, with a miniscule population of GATA3^{low} RORγt^{high} cells, each corresponding to ILC2s and ILC3s, respectively (Fig. 2F). In contrast to GATA3^{high} ILC2s in WT mice, those in ADAM10$^{\Delta Mx1}$ mice expressed RORγt. In line with this, GATA3^{high} ILC2s produced not only IL-5 and IL-13, but also IL-17 (Fig. S2H). Expression of these transcription factors and cytokine profiles was reminiscent of iILC2s, which is capable of inter-organ trafficking (Huang et al., 2015). iILC2s were dependent on IL-7 receptor, but not IL-15 receptor signaling, and alopecia phenotype remained unrescued in ADAM10$^{\Delta Mx1}$ *Il15ra*$^{-/-}$ mice (Fig. S2 I).

Differential expression of *Ccr2* and *Ccr6* between ILC1-NK cell cluster and ILC2-ILC3 cluster, respectively, prompted us to generate ADAM10$^{\Delta Mx1}$ mice in *Ccr2*$^{-/-}$ and *Ccr6*$^{-/-}$ backgrounds. Alopecia was markedly attenuated in ADAM10$^{\Delta Mx1}$ mice in *Ccr6*$^{-/-}$, but not in *Ccr2*$^{-/-}$ background (Fig. 2G). Lineage $^{-}$Thy1^{+} ILC numbers were decreased in ADAM10$^{\Delta Mx1}$ *Ccr6*$^{-/-}$ mice (Fig. 2H), which was due to prominent decreases in the numbers of GATA3^{high} RORγt^{mid} ILC2s (Fig. 2I). We further crossed ADAM10$^{\Delta Mx1}$ *Ccr6*$^{-/-}$ mice to the *Rag2*$^{-/-}$ background, in which *Ccr6*-deficiency is more specific to ILCs. In line with the results obtained in their *Rag2*-suffcient counterparts (Fig. 2G), ADAM10$^{\Delta Mx1}$ *Rag2*$^{-/-}$ *Ccr6*$^{-/-}$ mice harbored less GATA3^{high} RORγt^{mid} ILC2s and were

rescued from alopecia development (Fig. S2J). Consistent with this and the upregulation of the CCR6 ligand mRNA, *Ccl20*, by both uHFs and bulge cells in ADAM10$^{\Delta Mx1}$ mice (Fig. 1E, 1G), enzyme-linked immunosorbent assay revealed the abundance of CCL20 ADAM10$^{\Delta Mx1}$ mouse skin and to a lesser extent in the circulation (Fig. S2K). Local administration of an anti-CCL20 antibody for three consecutive days resulted in decreased GATA3^{high} RORγt^{mid} ILC2 numbers (Fig. S2L), demonstrating that they were recruited in a CCL20-CCR6 axis dependent manner.

In contrast to natural ILC2s that are tissue-residents, iILC2s are capable of entering circulation in a sphingosine-1 phosphate receptor (S1PR1)-dependent manner to migrate to sites of inflammation (Huang et al., 2018). To determine if GATA3^{high} RORγt^{mid} ILC2s were derived from circulation, we treated ADAM10$^{\Delta Mx1}$ mice with the S1PR1 inhibitor, FTY720. FTY720 administration led to a decrease in the numbers of GATA3^{high} RORγt^{mid} ILC2s and attenuated alopecia (Fig. 2J).

Taken together, these findings demonstrated that the inflammatory destruction of HFs in ADAM10$^{\Delta Mx1}$ mice was primarily mediated by IL-7 receptor-dependent iILC2s that circulated in an S1PR1-dependent manner that further infiltrated the skin and HFs in a CCR6-dependent manner, recruited by CCL20 produced by HFs that were immunologically activated as a result of ADAM10 ablation.

Destruction of the stem cell niche recapitulates cicatricial alopecia

Given the inflammatory alopecia phenotype in ADAM10$^{\Delta Mx1}$ mice, we further sought to determine if they reflected any aspects of alopecia areata or PCA (Anzai et al., 2019). Masson's trichrome staining revealed perifollicular fibrosis and lamellar hyperkeratosis of the hair canal (Fig. 3A). The CD200^{+} CD34^{+} bulge area was absent from ADAM10$^{\Delta Mx1}$ mouse HFs with reduction in bulge cell numbers from approximately 20 days post-induction (Fig. 3B, 3C). These features were reminiscent of those observed in PCA. Consistent with their reduced hair pigment, c-kit^{+} melanocytes and their CD34^{+} precursors (Joshi et al., 2019), which also reside in the bulge area (Nishimura et al., 2002), were decreased in ADAM10$^{\Delta Mx1}$ mice (Fig. 3D), suggesting that bulge destruction affected multiple stem cell lineages.

Downregulation of molecules that mediate the immune-privilege of HFs is implicated in immune-mediated alopecia (Harries and Paus, 2010; Rosenblum et al., 2004). To determine if a similar phenomenon was involved in our model, we sorted CD45^{-} non-immune cells from the skin of WT mice as well as from established alopecia lesions of ADAM10$^{\Delta Mx1}$ mice and subjected them to transcriptomic profiling via scRNA-seq. Unsupervised clustering analysis revealed 14 clusters that were identified based on their expressions of canonical markers (Fig. 3E, Table S4). Origin-based t-distributed stochastic neighbor embedding (t-SNE) plots validated that the bulge cluster was markedly decreased in ADAM10$^{\Delta Mx1}$ mice. Two distinct uHF clusters originated from WT (cluster 4) and ADAM10$^{\Delta Mx1}$ (cluster 2) mice, indicating transcriptomic shifts in the latter (Fig. 3E). DEG and pathway enrichment analysis in the uHF clusters highlighted upregulated pathways including positive regulation of cell death, epithelial proliferation, antigen presentation, and leukocyte migration, and downregulation of pathways including skin development and negative regulation of cell

proliferation (Fig. 3F, Table S5). Upregulated genes included those related to MHC II (*H2-ab1* and *Cd74*) and pro-inflammatory or antimicrobial peptides (*S100a8*, *S100a9*) and downregulated genes included immunoregulatory genes such as *Irf1*, *Id1*, *Socs3*, *Cish*, *Zfp36*, *Cd200* and the anti-microbial peptide gene, *Defb6* (Fig. 3G).

Immunofluorescence microscopy validated the upregulation of CD74 (Fig. 3H) and HF proliferation as determined via Ki-67 staining (Fig. 3I). Time-course analysis for MHC II and CD200 revealed that their expression in the uHFs was inversely correlated (Fig. 3J, 3K). Taken together, the upregulation of pro-inflammatory molecules and the downregulation of anti-inflammatory molecules demonstrated that ADAM10$^{\Delta Mx1}$ mouse uHFs had undergone immunological activation reminiscent of that observed in human immune-mediated alopecia.

Dysbiosis predominated by *Corynebacterium mastitidis* drives inflammatory alopecia

We further sought to validate our hypothesis that ADAM10 might play crucial roles in facilitating host-microbial symbiosis. Close examination of ADAM10$^{\Delta Mx1}$ mouse skin demonstrated adherence of whitish concretions in numerous HFs and hair shafts (Fig. 4A, upper panels), similar to that observed in trichomycosis, a human hair infection caused by *Corynebacterium* spp. (Almazán-Fernández and Fernández-Crehuet Serrano, 2017). Gram staining revealed bacteria-like elements in the uHFs (Fig. 4A, lower panels). Concretions stained positive for crystal violet, suggestive of biofilms, and propidium iodide staining revealed bacteria-like elements within (Fig. 4B, 4C). Skin swab cultures from ADAM10$^{\Delta Mx1}$ mice revealed increased microbial burden prior to alopecia onset at day 10 post-induction (Fig. 4D). Cultures of plucked hairs and isolated concretions yielded bacterial colonies that were identified as *C. mastitidis* via full-length 16S rRNA gene sequencing (Fig. 4D, S3A). Correspondingly, 16S rRNA gene amplicon sequencing performed on cells from skin swabs of WT and ADAM10$^{\Delta Mx1}$ mice revealed dysbiosis in the skin microbiome of ADAM10$^{\Delta Mx1}$ mice that was predominated by *Corynebacterium* spp. (Fig. 4E).

To determine whether dysbiosis was a prerequisite for the development of alopecia, ADAM10$^{\Delta Mx1}$ mice were treated orally with an antibiotic cocktail (Kobayashi et al., 2019) pre- and post-induction. This eradicated *C. mastitidis* as determined by microbiome analysis and skin swab cultures and rescued ADAM10$^{\Delta Mx1}$ mice from developing alopecia (Fig. 4E, 4F), suggesting that *C. mastitidis* predominance of the microbiota drove the alopecia phenotype. ILC2s and CD4^{+} T cells were significantly reduced in antibiotic-treated ADAM10$^{\Delta Mx1}$ mice with normalized RORγt expression in the former (Fig. 4G), denoting that inflammation followed dysbiosis. Notably, normal HF structures and bulge cells (Fig. 4H) and melanocyte numbers (Fig. 4I) were retained in antibiotic-treated ADAM10$^{\Delta Mx1}$ mice, indicating that the alopecia phenotype was not due to structural alteration in the absence of ADAM10, but due to dysbiosis-triggered inflammation.

Whereas oral antibiotics suppressed *C. mastitidis* and prevented alopecia, discontinuation of treatment at day 30 post-induction led to a re-emergence of *C. mastitidis* followed by alopecia onset, supporting the link between this dysbiotic flora with the phenotype (Fig. S3B). Treating ADAM10$^{\Delta Mx1}$ mice with antibiotics after alopecia onset did not rescue the phenotype (Figure S3C), consistent with the loss of the bulge structure and validating the irreversible nature of hair loss in this model.

Systemic antibiotics might globally affect the microbiome and host immunity. The *Mx1* promoter remained active in antibiotic-treated ROSA26YFP$^{\Delta Mx1}$ mice as determined by YFP-positivity in uHFs (Fig. S3D), excluding the possibility that antibiotics may attenuate type I IFN responses directly or indirectly by modulating inflammation or by decreasing the load of bacteriophage-carrying bacterium, respectively. To specifically target the skin microbiota, we treated ADAM10$^{\Delta Mx1}$ mice with a topical antibiotic cream containing neomycin, bacitracin and polymyxin, which enables depletion of the local bacterial flora (Di Domizio et al., 2020). Indeed, topical antibiotics eradicated *C. mastitidis* and markedly attenuated alopecia (Fig. S3E). To further solidify the role of *C. mastitidis* in driving the alopecia phenotype, WT and ADAM10$^{\Delta Mx1}$ mice were pre-conditioned with oral antibiotics until poly(I:C) injection and were then inoculated with *C. mastitidis* or vehicle. *C. mastitidis*-inoculated ADAM10$^{\Delta Mx1}$ mice showed increased *C. mastitidis* load and an early onset of alopecia at day 10 post-induction (5 days post-inoculation) and displayed maximal phenotype at day 25 (20 days post-inoculation), the severity of which was comparable to ADAM10$^{\Delta Mx1}$ mice at day 40 post-induction (Fig. 4J, Fig. 2A). These data demonstrated that *C. mastitidis* enhanced HF inflammation and accelerated alopecia onset (Fig. 4J). Neither co-housing WT mice with ADAM10$^{\Delta Mx1}$ mice, nor the inoculation of *C. mastitidis* on WT, *Rag2*$^{-/-}$ or *Il7ra*$^{-/-}$ led to alopecia (Fig. S3F, S3G, Fig. 4J), indicating that the lack of *Adam10* was crucial for *C. mastitidis* to colonize and to drive pathological inflammation.

Because alteration of the gut microbiome could potentially have immunological effects on distant sites (e.g. skin), we analyzed the gut of ADAM10$^{\Delta Mx1}$ mice. Their gut remained grossly and histologically normal, and microbiome analysis revealed comparable profiles to that of WT control mice (Fig S4A-S4C), suggesting that a gut-skin immune axis was unlikely to be involved in this model.

Thus, skin dysbiosis predominated by *C. mastitidis* was essential for driving the inflammatory destruction of HFs in ADAM10$^{\Delta Mx1}$ mice.

Dysbiosis and inflammation trigger immunological activation of HFs

To determine the hierarchical roles of dysbiosis and the immunological activation of HFs in triggering alopecia, we performed scRNA-seq on CD45^{-} cells from WT and ADAM10$^{\Delta Mx1}$ mice with or without antibiotics and identified 17 distinct clusters (Fig. 5A, Table S6). Consistent with the initial analysis (Fig. 3E), origin-based t-SNE plots revealed two distinct clusters of uHFs. The majority of WT uHFs were non-inflammatory, whereas the majority of those from ADAM10$^{\Delta Mx1}$ mice were inflammatory, as represented by the differential expression of *H2-Ab1*. Notably, a large proportion of inflammatory uHFs was suppressed in antibiotic-treated ADAM10$^{\Delta Mx1}$ mice (Fig. 5B, 5C), indicating that this subset in ADAM10$^{\Delta Mx1}$ mice underwent proliferation in response to dysbiosis, consistent with their upregulated pathway for epithelial cell proliferation and increased Ki-67 expression (Fig. 3F, 3I). Heatmap for top DEGs revealed that antibiotics normalized the expressions of pro-inflammatory genes and partially rescued the expressions of genes involved in immune regulation or HF homeostasis (Fig. 5D, Table S7). Flow cytometry validated that frequencies of MHC II^{+} uHF cells in ADAM10$^{\Delta Mx1}$ mice was suppressed by antibiotics treatment (Fig.

5E). In contrast to ADAM10$^{\Delta Mx1}$ mice and ADAM10$^{\Delta Mx1}$ *Rag2*$^{-/-}$ mice, which exhibited alopecia, frequencies of MHC II^{+} uHF cells were reduced in ADAM10$^{\Delta Mx1}$ mice in *Ccr6*$^{-/-}$ or *Il7ra*$^{-/-}$ backgrounds and in FTY720-treated ADAM10$^{\Delta Mx1}$ mice, indicating that immune cell infiltration was crucial for immunological activation of the HFs (Fig. 5F). These data demonstrated that immunological activation of the HFs was a secondary event that could be prevented by targeting the dysbiotic flora or iILC2s in ADAM10$^{\Delta Mx1}$ mice.

ADAM10-Notch signaling axis regulates dysbiosis

ADAM10 regulates various biological processes, including the Notch signaling pathway (Edwards et al., 2008). Indeed, Notch signaling pathway was downregulated in *Adam10*-ablated uHFs (Fig. 1E, 1F, Table S1). Thus, to determine if impaired Notch signaling underlies the alopecia phenotype, we generated RBPJ$^{\Delta Mx1}$ mice in which Notch signaling is impaired (Tanigaki et al., 2002), as well as ADAM10$^{\Delta Mx1}$xROSA^{NICD}mice, in which *Adam10*-ablated cells simultaneously underwent forced expression of NICD, thereby bypassing the requirement for *Adam10* during Notch signaling (Murtaugh et al., 2003). RBPJ$^{\Delta Mx1}$ mice developed alopecia which phenocopied ADAM10$^{\Delta Mx1}$ mice, whereas ADAM10$^{\Delta Mx1}$xROSA^{NICD} mice displayed attenuated phenotypes (Fig. 6A). These data established impaired Notch signaling as the major pathway downstream of ADAM10 underlying the inflammatory alopecia phenotype.

The above data and the critical involvement of *C. mastitidis* in the development of alopecia in ADAM10$^{\Delta Mx1}$ mice (Fig. 4) suggested that Notch signaling downstream of ADAM10 regulated dysbiosis. Indeed, skin swab cultures revealed high bacterial burdens in RBPJ$^{\Delta Mx1}$ mice (Fig. 6B). Furthermore, microbiome analysis revealed that their skin microbiome was predominated by *Corynebacterium* spp. recapitulating that of ADAM10$^{\Delta Mx1}$ mice (Fig. 6C). Moreover, antibiotic treatment in RBPJ$^{\Delta Mx1}$ mice prevented alopecia, reduced the frequencies of MHC II^{+} uHF cells, and preserved the bulge area (Fig. 6D, 6E). These data demonstrated the ADAM10-Notch signaling axis to be a crucial regulator of the HF microbiome. Despite their rescued phenotype, ADAM10$^{\Delta Mx1}$*Ccr6*$^{-/-}$ mouse skin microbiome was predominated by *Corynebacterium* spp. (Fig. 6B, 6C), indicating that dysbiosis alone was insufficient to induce alopecia and it required inflammatory destruction of HFs by iILC2s, consistent with our previous findings (Fig. 2).

Having identified dysbiosis as the primary event leading to alopecia, we hypothesized that inhibition of the ADAM10-Notch signaling axis might lead to impaired epithelial innate immunity against *Coyrnebacterium* spp. Thus, we performed scRNA-seq on cells from RBJP$^{\Delta Mx1}$ mouse skin and took a reductional approach to investigate genes that were regulated downstream of this axis. First, we identified 2452 Notch-dependent genes via comparison of DEGs between WT and ADAM10$^{\Delta Mx1}$ and those between WT and RBJP$^{\Delta Mx1}$ mouse uHFs (Fig. 6F, upper panel, Table S7). Comparison of DEGs between WT and ADAM10$^{\Delta Mx1}$ to those between antibiotic-treated or - untreated ADAM10$^{\Delta Mx1}$ mice yielded 895 genes whose transcriptomic changes were unlikely to be secondary to inflammation, antibiotics, or dysbiosis (Fig. 6F, middle panel, Table S8). Next, by comparing the Notch-dependent gene and non-secondary gene lists, we identified 286 core genes that were downstream of the ADAM10-Notch signaling axis (Fig. 6F, lower

panel, Table S9). Upregulated genes included those that were initially identified as highly expressed in ADAM10$^{\Delta Mx1}$ mice, such as those involved in antigen presentation (e.g., MHC II genes, *Cd74*) and inflammatory or anti-microbial responses (Fig. 6G, 6H). We found *Defb6* to be the only downregulated antimicrobial peptide gene (Fig. 6G). Relevant genes involved in toll-like receptor (TLR) signaling, a critical machinery for host recognition of bacterial components, were downregulated (*Fos*, *Jun*, *Myd88*, *Map3k8*) (Fig. 6G, 6H).

To characterize the type I IFN response that was induced by poly(I:C) injection and the potential alteration of this response in the absence of ADAM10-Notch signaling, we injected WT mice once with poly(I:C) and harvested uHF cells 24 hours later for bulk RNAseq. DEGs as compared to uninjected WT mice included typical type I IFN responsive genes (Table S10). Comparison of the DEG set from the infundibulum with the 286 core ADAM10-Notch genes revealed 51 overlappping genes, with 28 dysregulated genes that were expressed in opposite directions in ADAM10$^{\Delta Mx1}$ and RBPJ $^{\Delta Mx1}$ mice as compared to WT mice (Table S10, Fig. 6I). Notably, these analyses revealed that the expression of relevant genes such as *Cd200* and *Defb6* to be induced by type I IFN, which response was impaired in the absence of ADAM10-Notch signaling axis (Fig. 6I).

Defb6 expression is enriched in mouse uHFs (Joost et al., 2016) and its downregulation in ADAM10$^{\Delta Mx1}$ and RBJP$^{\Delta Mx1}$ mice (Table S3) suggested mBD-6 to be a regulator of skin commensal microbes at the follicular opening. mBD-6 possesses antimicrobial activity against *E. coli* (Yamaguchi et al., 2002), but its activity against skin microbes is uncharacterized. Hence, we assessed its bactericidal activity against *C. mastitidis* isolated from ADAM10$^{\Delta Mx1}$ mice, in comparison with mBD-1, which was upregulated in ADAM10$^{\Delta Mx1}$ mouse uHFs (Table S5), as well as human β-defensin (hBD)-1 and hBD-3 which are prototypic anti-microbial peptides with potent bactericidal activities against Gram-negative and -positive bacteria, respectively (Ali et al., 2001; Harder et al., 2001). As anticipated, mBD-6 displayed potent bactericidal activity against *C. mastitidis* that was superior than that of mBD-1 and hBD-1 and was comparable to that of hBD-3 (Fig. 6J).

Consistent with our sequence data (Fig. 6G, 6I, Table S5), treatment of isolated uHF keratinocytes with *Adam10* siRNA led to decreased *Defb6* expression (Fig. 6K). We further utilized a mouse keratinocyte cell line, MPEK-BL6, and co-culturing it with heat-killed *C. mastitidis* (HKCM) led to increased *Defb6* expression (Fig. 6L). In contrast, knockdown of either *Adam10* or *Rbpj* abolished this response, validating that *Defb6* upregulation required the ADAM10-Notch signaling axis. In addition to *Myd88* (Fig. 6G, 6H), a critical adaptor protein that mediates most TLR signaling, *Tlr5* was downregulated in ADAM10$^{\Delta Mx1}$ mouse uHFs (Table S1). Therefore, we treated MPEK-BL6 cells with siRNA against *Myd88*, *Tlr5*, and *Tlr2*, as TLR2 has a role in recognizing peptidoglycans in gram-positive bacterial cell wall (Takeuchi and Akira, 2010). This demonstrated that MyD88, TLR2, and TLR5 were all required for *Defb6* upregulation in response to HKCM (Fig. 6M), suggesting that HKCM recognition involved the coordination of both TLR2 and TLR5. Topical application of mBD-6 in ADAM10$^{\Delta Mx1}$ mice was sufficient to suppress *C. mastitids* colonization and mitigated alopecia development (Fig. 6N).

Thus, *Defb6* was expressed downstream of the ADAM10-Notch signaling axis, further induced by HKCM exposure in a TLR-MyD88 signaling-dependent manner. mBD-6 exhibited potent activity against *C. mastitidis in vitro* and *in vivo*, the topical application of which was sufficient to attenuate the alopecia phenotype, supporting that the ADAM10-Notch signaling axis bolstered the innate epithelial barrier by mediating the expression of *Defb6* at the follicular opening, thereby regulating the expansion of *C. mastitidis*.

HF destruction and pyroptosis is mediated by inflammatory caspases

In contrast to apoptosis, pyroptosis is a lytic form of cell death occurring in response to microbial stimuli, leading to the release of pro-inflammatory cytokines, primarily IL-1α and IL-1β, thereby alarming local immunity (Kesavardhana et al., 2020). Pyroptosis is mediated by inflammatory caspases, caspase-1, −4, −5, and −12 in humans. In mice, caspase-11 represents human caspase-4 and −5 (herein referred to as caspase-4;11) (Abu Khweek and Amer, 2020). Caspase-1 requires the assembly of inflammasomes to be cleaved into active forms, whereas caspase-4;11 is capable of sensing lipopolysaccharide from gram-negative bacteria and undergoing direct activation (Shi et al., 2014). Caspase-1 is required for the release of IL-1β and IL-18, whereas caspase-4;11 is required for IL-1α release (Casson et al., 2013).

Pathway analysis on bulk RNA-seq data for HF subsets prior to alopecia onset suggested enhancement of cell death programs, wherein the upregulation of *Casp4* and *Il1a* in the uHFs and *Casp1* and *Il1b* in the bulge pointed to pyroptosis as the possible mechanism (Fig. 1E-1H). We detected caspase-1, −4;11, and pore-forming gasdermins A and C, but not caspase-3, in ADAM10$^{\Delta Mx1}$ mouse HFs via immunofluorescence and immunohistochemical microscopy, suggesting a pyroptotic process rather than apoptosis (Fig. 7A). Western blot analysis on CD45^{-} mouse epidermal cells isolated from ADAM10$^{\Delta Mx1}$ mice validated increased caspase-1, −4;11 and, gasdermins A and C (Fig. 7B).

To further study this *in vitro*, we treated MPEK-BL6 cells with a cocktail of ILC-derived cytokines (IL-5, IL-13, IL-17, amphiregulin, and bone morphogenetic protein 2) (Table S2, Fig. S2G, S2H), HKCM, or both. Microscopy revealed that the cytokine cocktail increased cellularity but did not affect keratinocyte morphology. Treatment with HKCM triggered cell swelling and bubble-like changes, which was accentuated in those treated with HKCM and the cytokine cocktail (Fig. 7C). These morphological features were consistent with pyroptosis (Hou et al., 2020). Either HKCM alone or HKCM + cytokine cocktail triggered the upregulation of *Casp4* expression (Fig. 7D). *Casp1* was undetected, suggesting that MPEK-BL6 cells shared features with uHFs, but not bulge cells. Consistent with this expression pattern, HKCM induced the release of IL-1α, but not IL-1β or IL-18 into the culture supernatant, which was augmented by the cytokine cocktail (Fig. 7E). Treatment of MPEK-BL6 cells with the caspase-4 inhibitor, Z-YVAD-FMK, suppressed HKCM + cytokine-mediated release of IL-1α (Fig. 7F). These data demonstrated that MPEK-BL6 cells underwent pyroptotic cell death that was mediated by caspase-4;11 in response to HKCM, which was augmented by ILC-derived cytokines.

Finally, to determine if inflammatory caspases executed HF destruction *in vivo*, ADAM10$^{\Delta Mx1}$ mice were treated with caspase inhibitors. Notably, pan-caspase, caspase-1,

and caspase-4;11 inhibitors all attenuated alopecia phenotype (Fig. 7G). These *in vitro* and *in vivo* data confirmed that HF destruction in ADAM10$^{\Delta Mx1}$ mice was mediated by inflammatory caspases-1 and −4;11 that promote pyroptosis.

Collectively, the inhibition of ADAM10-Notch signaling axis during an experimentally induced anti-viral immunity resulted in the breakdown of the innate epithelial barrier in the uHFs, enabling the predominance of *C. mastitidis*. Dysbiosis triggered inflammation mediated by iILC2s, which resulted in the inflammatory destruction of the HFs and its stem cell niche, which was ultimately executed by the inflammatory caspases-1 and −4;11.

Discussion

Type I IFN responses in epithelial cells represent the first line of defense that triggers host-protective immunity (McNab et al., 2015). However, such exuberant type I IFN responses are not without consequences and can precipitate or exacerbate autoimmune disease (Adler and Christopher-Stine, 2018; Filippi and von Herrath, 2008; Illescas-Montes et al., 2019; Ito and Tokura, 2012; Rodriguez and Duvic, 2008) or render the host susceptible to subsequent bacterial infections (Manohar et al., 2020). While commensal microbes critically contribute to the maintenance of host immunity, tissue repair and metabolism, their pervasiveness needs to be controlled throughout homeostasis and inflammation to preserve normal tissue functions. The failure to regulate commensal microbes can result in perpetuating tissue inflammation, such as those observed in atopic dermatitis and cystic fibrosis (Geoghegan et al., 2018; Yi et al., 2021). Our data presented herein highlight the impact systemic type I IFNs have on the epidermis, particularly in the uHFs, and how a coordinated innate epithelial response mediate by ADAM10-Notch signaling axis is required to control the local microbiome and inflammation.

Defensins are small cationic peptides that are expressed in a variety of cell types and are curators of pervasive commensal microbial loads (Meade and O'Farrelly, 2019). β-defensins are the most extensively studied subtype with a wide range of species-specific genes that have been identified (Semple et al., 2005), suggesting that distinct microbial pressure in different mammalian species have led to the evolutionary diversification of β-defensins. Notably, the activity of β-defensins are not limited to bacteria but also extend to viral, fungal and parasitic agents (Chessa et al., 2020; Cobo and Chadee, 2013; Klotman and Chang, 2006; Silva et al., 2014). We found that systemic poly(I:C) injection triggered the upregulation of *Defb6* in the uHFs from WT mice, suggesting this response to be an integral component during a type I IFN response that likely regulates untoward expansion of microbial agents. *Defb6* response relied on the ADAM10-Notch signaling axis, the inhibition of which led to an alteration of the skin microbiota that was predominated by *C. mastitidis*. Anti-microbial activities of β-defensins have been mostly validated *in vitro*, with very few validation *in vivo* (Meade and O'Farrelly, 2019). Our demonstration that topical application of synthetic mBD-6 was sufficient to suppress *C. mastitidis*-mediated dysbiosis in ADAM10$^{\Delta Mx1}$ mice, highlights its central role in regulating microbes at the follicular opening and further provides a premise for the use of topical β-defensins to harness the skin commensals.

In addition to topical mBD-6, effective targeting of *C. mastitidis* with either oral or topical antibioitics markedly prevented the development of alopecia. Furthermore, the inoculation *C. mastitidis* onto antibiotic pre-conditioned ADAM10$^{\Delta Mx1}$ mice enhanced and maximized alopecia phenotype, demonstrating that dysbiosis predominated by *C. mastitidis* to be an essential component that triggered follicular inflammation in ADAM10$^{\Delta Mx1}$ mice. This was reminiscent of our previous observation in *Sox9*-Cre x *Adam17*$^{f/f}$ mice, in which the constitutive ablation of *Adam17* in the epidermis led to skin-surface dysbiosis predominated by *S. aureus* that drove atopic skin inflammation. Therefore, these two relevant members of the ADAM family, ADAM10 and ADAM17, play major roles in regulating follicular and skin-surface microbiota, respectively. Notably, ADAM17 regulates skin-surface *S. aureus* via epidermal growth factor receptor signaling (Kobayashi et al., 2015), whereas ADAM10 utilized Notch signaling to regulate *C. mastitidis* in the follicular compartment, demonstrating that these skin compartments leverage distinct mechanisms to regulate the microbiota. Ablation of *Adam10* in the uHFs in ADAM10$^{\Delta Mx1}$ mice caused *Adam10*-unablated bulge keratinocytes to undergo immunological activation and functional alteration, suggesting that uHF homeostasis is crucial for the bulge to maintain its function. Presumably, tightly regulated signals derived from the uHFs trigger bulge activation and proliferation of hair regeneration to bolster the skin barrier system and to expel unwanted microbial agents. Functional ADAM10-Notch signaling axis is required for this process, and future identification and characterization of uHF-derived signaling molecules would deepen our understanding of how the HF unit coordinates antimicrobial responses. While the contribution of IFE cannot be completely ruled out given their type I IFN responsiveness, the alopecia phenotype was recapitulated in ADAM10$^{\Delta Lrig1}$ mice, indicating that ablation of Adam10 specifically from uHFs were sufficient to induce the phenotype.

While it is still premature to suggest if the phenomena we observe in ADAM10$^{\Delta Mx1}$ mice exist in human alopecia, it may be analogous to pathophysiology involved in atopic dermatitis. *S. aureus* alone is insufficient to drive atopic inflammation but rather, it drives inflammation in the context of genetic alterations of the epidermal barrier (Kubo et al., 2012). It is attractive to hypothesize that genetic alterations along the ADAM10-Notch signaling axis renders susceptibilities to hair loss diseases, especially PCA, for which treatment options are limited. Thus, it would be clinically relevant to investigate whether follicular dysbiosis is associated with subtypes PCA, and whether HF destruction involves ILCs and inflammatory caspases, which would open up avenues for the development of future therapeutic strategies. Of note, oral antibiotics are utilized to limit progression in CCCA (Whiting and Olsen, 2008), and the CD4^{+} T cell-rich infiltrate resembles that of ADAM10$^{\Delta Mx1}$ mice. It may be worthwhile exploring if ILCs can be identified in CCCA lesions.

In summary, we demonstrated ADAM10-Notch signaling axis to be a crucial regulator of the microbiota at the follicular opening, disruption of which led to dysbiosis predominated by *C. mastitidis*, triggering ILC-mediated inflammatory destruction of the HFs and its stem cell niche which involved pyroptosis, ultimately resulting in irreversible alopecia. These data propose that regulation of host-microbial symbiosis is crucial for tissue and stem cell homeostasis, which has clinical implications for sustaining tissue integrity during chronic inflammation. Our findings also provide impetus for exploring the host-microbial axis as a

potential driver of pathophysiology in human PCA and to pursue the development of future therapeutic strategies.

Limitations of the study

Although we have shown that dysbiosis in ADAM10-Notch signaling axis ablation models is due to the downregulation of *Defb6*, it is unclear why *C. mastitidis* displays predominance over other species. We speculate that this might reflect the propensity of *Corynebacterium* species to colonize the HFs and hair shafts. It is also possible that like in humans, mice also display distinct microbial compositions in different anatomical sites, which could potentially explain the predilection of alopecia onset in the chest area in the mouse models studied herein. Notably, human PCA subtypes also exhibit predilection for certain sites of the scalp (e.g. vertex in CCCA or frontal areas in frontal fibrosing alopecia). It remains to be explored if the mouse models described in this study reflects aspects of PCA. We demonstated that iILC2s were required for the development of alopecia, but the detailed mechanisms by which iILC2s induce pyroptotic cell death of HFs has yet to be determined.

STAR Methods

RESOURCE AVAILABILITY

Lead contact—Further information and requests for resources and reagents should be directed to, and will be fulfilled by, the Lead Contact, Keisuke Nagao (keisuke.nagao@nih.gov)

Materials availability—*C. mastitidis* strain generated in this paper is available upon request.

Data and code availability

- RNA and microbiome sequence data have been deposited at GEO and BioProject, respectively, and are publicly available as of the date of publication. Accession numbers are listed in the key resources table.
- This paper does not report original code.
- Any additional information required to reanalyze the data reported in this paper is available from the lead contact upon request.

Experimental Models and Subject Details

Mice—Mice were bred and/or maintained in the NIAMS specific pathogen-free facility in accordance with the Guide for the Care and Use of Laboratory Animals. All experiments were performed at NIAMS under an animal study proposal approved by the NIAMS Animal Care and Use Committee. 4- to 12-week-old female mice were used for each experiment. *Adam*$10^{f/f}$ mice were generated as previously described (Yoda et al., 2011). B6.Cg-Tg(Mx1-cre)1Cgn/J (Mx1-Cre mice), B6.129X1-Gt(ROSA)$^{26Sortm1(EYFP)Cos}$/J (ROSA26YFP mice), Lrig1$^{tm1.1(cre/ERT2)Rjc}$/J (Lrig1-creERT mice), B6;SJL-Tg(Krt1-15-cre/PGR)22Cot/J (K15-crePGR mice), B6(Cg)-*Rag2*$^{tm1.1Cgn}$/J (*Rag2*$^{-/-}$ mice), B6.129S4-*Ccr2*^{tm1Ifc}/J (*Ccr2*$^{-/-}$

mice), B6.129P2-*Ccr6*^{tm1Dgen}/J (*Ccr6*$^{-/-}$ mice), B6.129S7-Il7r^{tm1Imx}/J (*IL7ra*$^{-/-}$ mice) and Gt(ROSA)$^{26Sortm1(Notch1)Dam}$/J (NICD mice) were purchased from The Jackson Laboratory. C57BL/6NTac.Cg-Rag2tm1Fwa Il2rgtm1Wjl(Rag2$^{-/-}$ Il2rg$^{-/-}$ mice) were purchased from Taconic Biosceineces. ROSA26YFP mice were cross-bred with Mx1-Cre mice, Lrig1-creERT mice or K15-crePGR mice to obtain ROSA26YFP$^{\Delta Mx1}$ mice, ROSA26YFP$^{\Delta Lrig1}$ mice, ROSA26YFP$^{\Delta K15}$mice respectively. ROSA26YFP$^{\Delta Mx1}$, ROSA26YFP$^{\Delta Lrig1}$ or ROSA26YFP$^{\Delta K15}$ mice were further crossed to *Adam10*$^{f/f}$ mice to generate ADAM10;ROSA26YFP$^{\Delta Mx1}$ mice, ADAM10;ROSA26YFP$^{\Delta Lrig1}$ mice or ADAM10;ROSA26YFP$^{\Delta K15}$ mice. *Adam10*$^{f/f}$ mice were cross-bred with Mx1-Cre mice to obtain ADAM10$^{\Delta Mx1}$ mice. ADAM10$^{\Delta Mx1}$ mice were further crossed with *Rag2*$^{-/-}$, *Ccr2*$^{-/-}$, *Ccr6*$^{-/-}$, *Il7ra*$^{-/-}$, Csf1r-cre or NICD mice to generate ADAM10$^{\Delta Mx1}$ *Rag2*$^{-/-}$ mice, ADAM10$^{\Delta Mx1}$ *Ccr2*$^{-/-}$ mice, ADAM10$^{\Delta Mx1}$ *Ccr6*$^{-/-}$ mice, ADAM10$^{\Delta Mx1}$ *Il7ra*$^{-/-}$, ADAM10$^{\Delta Csf1r}$ mice or ADAM10$^{\Delta Mx1}$ NICD mice respectively. Rbpj^{tm1Hon} mice (Tanigaki et al., 2002) was a kind gift originally from Tasuku Honjo (Kyoto University, Japan) and then provided by Hidehiro Yamane (NCI, NIH). *Rbpj*^{tm1Hon} mice were cross-bred with Mx1-Cre mice to obtain RBPJ$^{\Delta Mx1}$ mice.

Method Details

Polyinosinic–polycytidylic acid (poly(I:C)) injection—Cre activation was induced by injecting 4 to 5-week-old mice intraperitoneally with 200 μg of poly(I:C) (InvivoGen, Cat# vac-pic) in 200 μl saline, every other day for a total of three doses. All mice were harvested 30 - 40 days post-induction unless specified otherwise.

Tamoxifen and RU486/mifepristone injection—Cre activation in *Lrig1*-creERT mice was induced by injecting 4 to 5-week-old mice intraperitoneally with 75 mg/kg (high dose) or 10 mg/kg (low dose) of tamoxifen (Sigma) in sunflower oil, twice a week for a total of three doses. Cre activation in *K15*-crePGR mice was induced by injecting 4 to 5-week-old mice intraperitoneally with 200mg/kg RU486/mifepristone (Sigma) in sunflower oil, every other day for a total of three doses. All mice were harvested 30 - 40 days post-induction unless specified otherwise.

Antibody treatment—Thy1.2 (IgG2b, clone 30H12; Bio X cell) or isotype control (IgG2b, clone LTF-2; Bio X cell) were administered subcutaneously in ADAM10$^{\Delta Mx1}$ *Rag2*$^{-/-}$ mice into the upper chest area twice weekly at a dose of 250 μg /mouse starting at day 0 of poly(I:C) administration. Mouse CCL20/MIP-3 alpha Antibody (R&D) or isotype control (IgG1 Isotype control) were administered subcutaneously in ADAM10$^{\Delta Mx1}$ mice into the upper chest area at a dose of 100 ug/mouse for 3 days starting at day 17 of poly(I:C) administration.

Antibiotic treatment—For oral antibiotics treatment, mice were continuously fed 0.5mg/mL of cefazolin (WG Critical Care) and 0.5mg/mL of enrofloxacin (Bayer) in their drinking water (Kobayashi et al., 2019). For topical treatment, the chest area of mice were treated once daily with 0.05 g topical triple antibiotic ointment containing neomycin, bacitracin, and polymyxin or the same amount of Vaseline.

FTY720 (Fingolimod) and caspase inhibitor administration—Mice were treated intraperitoneally with 3mg/kg of FTY720 (Shelleckchem) starting one day before poly(I:C) injection and twice weekly for the duration of the experiment. Mice were treated intraperitoneally with 8mg/kg of either pan-caspase inhibitor (Z-VAD-FMK), caspase-1 inhibitor (Ac-YVAD-cmk) or caspase-4 inhibitor (Z-YVAD-FMK) (Invivogen) dissolved in 5% DMSO in 200 μl PBS one day before poly(I:C) injection and twice weekly for the duration of the experiment.

Synthetic mouse β-defensin-6 treatment—The chest area of mice were treated with 200ug/ml of synthetic mBD-6 in 50 ul water or the same amount of water starting one day before poly(I:C) injection and three times a week for the duration of the experiment.

Bone marrow transplantation—2×10^6 of bone marrow cells from poly(I:C) induced WT and ADAM10$^{\Delta Mx1}$ mice were transferred intravenously into lethally irradiated (9.5 Gy) 4-week-old ADAM10$^{\Delta Mx1}$ and WT mice respectively. 8 weeks after bone marrow transplantation, mice were additionally injected poly(I:C) and were harvested 40 days post-induction with poly(I:C).

T cell and ILC reconstitution—To reconstitute T cells, 2×10^6 of skin-draining lymph node cells from poly(I:C) induced WT and ADAM10$^{\Delta Mx1}$ mice were transferred intravenously into unirradiated *Rag2*$^{-/-}$ mice, respectively, and were additionally treated with one-time poly(I:C) injection. To reconstitute ILCs, 2×10^6 of bone marrow cells from poly(I:C) induced WT and ADAM10$^{\Delta Mx1}$ mice were transferred intravenously into unirradiated *Rag2*$^{-/-}$*Il2rg*$^{-/-}$ mice, respectively, and were additionally treated with one-time poly(I:C) injection and harvested 4 weeks after. At this time point, ILCs but not T cells fully reconstituted in *Rag2*$^{-/-}$*Il2rg*$^{-/-}$ mice.

Tissue processing—Skin cell suspensions were prepared from mouse chest skin. Harvested whole skin samples were placed in PBS on ice. Subcutaneous tissues were mechanically removed with forceps. To obtain epidermal cell suspensions, harvested skin was floated on 10 mL of 0.15% trypsin and 0.75 mM EDTA (a mixture of 5 mL of 0.25% Trypsin-1mM EDTA and 5 mL of 0.05% Trypsin-0.5mM EDTA) (GIBCO) and incubated at 37°C for 45 min. The epidermis was then scraped off with forceps into PBS containing 5% fetal bovine serum (FBS) (BenchMARK™). The cell suspension was further mechanically dissociated with a 50 ml syringe (Covidien) and then filtered through a sterile 100 μm Falcon® Cell Strainer (Corning). The cells were washed with PBS containing 5% FBS and further filtered through a 40 μm Falcon® Cell Strainer (Corning) into a new 50 ml conical tube. To obtain whole skin cell suspensions, harvested skin was minced with scissors in 5 mL of RPMI containing 0.25 mg/mL of Liberase TL Research grade (Roche) and 1 μg/mL of DNase I (Sigma) in 6 well plates and were incubated at 37°C for 2 hours. 1 mL of 0.25% Trypsin-1 mM EDTA was added into each well for the last 10 minutes of incubation. Reaction was stopped by adding 4ml PBS containing 5% FBS into each well. Cell suspensions were further mechanically dissociated with a 12 ml syringe (Covidien) and were then filtered through a sterile 100 μm Falcon® Cell Strainer. The cells were washed

with PBS containing 5% FBS and were then filtered through a 40 μm Falcon® Cell Strainer into a new 50ml conical tube.

***In vitro* re-stimulation—**For detection of cytokine production, single cell suspensions were cultured *ex vivo* in 96-well plates in 200μl of complete RPMI (RPMI 1640 supplemented with 10% FBS, 1 mM sodium pyruvate and non-essential amino acids, 100 U/mL penicillin, 100 μg/mL streptomycin, 0.25 μg/mL of Amphotericin B and 50 mM β-mercaptoethanol) and were stimulated with Leukocyte Activation Cocktail, with BD GolgiPlug™ for 4 hours at 37°C in 5% CO_2. After stimulation, cells were used for intracellular cytokine staining to be analyzed via flow cytometry

Flow cytometry analysis—Cells were stained with Zombie Aqua Fixable Viability Kit (BioLegend) for 20 min at RT, were incubated with anti-mouse CD16/32 antibody (BioLegend) to block Fc receptors and were then incubated primary antibodies for 30 min on ice. The data was acquired by LSR ll or LSR Fortessa (BD Biosciences) and analyzed by using FlowJo software (FlowJo, LLC). Zombie Aqua-stained dead cells and doublet cells were removed from the analysis. Lymphoid lineages were identified as $CD45^+Thy1.2^+$. γδ T cells were distinguished into $TCR\gamma\delta^{high}$ and $TCR\gamma\delta^{mid}$ populations. $TCR\gamma\delta^-$ cells were gated for CD4 and CD8 to identify $CD4^+$ and $CD8^+$ T cells. $CD4^-CD8^-$ cells were then separated into $CD2^+$ NK cell or ILC1 populations and $CD2^-$ ILC populations that include ILC2s and ILC3s. To directly quantify ILCs, $CD45^+$ $lineage^-$ ($CD3\varepsilon^-$, $CD11b^-$, $CD11c^-$, $CD5^-$, $CD19^-$, $Fc\varepsilon RI\alpha^-$, $NK1.1^-$ and $CD2^-$) $Thy1.2^+$ cells were gated. From the $CD45^+$ $lineage^-$ (Siglec-F^-, $CD3\varepsilon^-$, $CD19^-$ and $NK1.1^-$) gate, $CD11b^+Ly6c^+$ cells were identified as monocytes, $Ly6c^-CD64^-EpCAM^+$ as Langerhans cells, $Ly6c^-EpCAM^-CD64^+$ cells as macrophages and further $CD11c^+$MHC II^+ cells as dendritic cells. For transcription factor and cytokine staining, cells were fixed and permeabilized with Foxp3/Transcription Factor Staining Buffer Set (eBioscience) and were incubated with anti-transcription factor antibodies or anti-cytokine antibodies for overnight at 4°C.

Sample collection for bacterial culture—Samples were collected from the face, neck and chest area with sterile foam swabs (Puritan, 25-1506 1PF) pre-moistened with PBS and were suspended in 200 μl of PBS. Neat, 1:10–1:1000 dilutions were cultured on Tryptic Soy Agar with 5% sheep blood plates (Thermo Fisher Scientific) for 48 hours. Hair was plucked from chest area and cultured on Tryptic Soy Agar with 5% sheep blood plates for 48 hours. Concretions were isolated from hair shafts carefully with sterile precision tweezers under a dissecting microscope. Concretions were then cultured on Tryptic Soy Agar with 5% sheep blood plates for 96 hours.

Preparation of heat-killed *C. mastitidis* (HKCM)—*C. mastitidis* was isolated from $ADAM10^{\Delta Mx1}$ mice skin. Single colony was transferred onto BHI broth supplemented with 0.1% Tween 80 and cultured in shaking incubator at 37°C at 120 rpm for 48h at which absorbance of 0.1 O.D. at A600 nm corresponded to $7x10^7$ CFU/ml. After washing cells were resuspended in PBS and were heat-killed in a water bath at 70°C for 30 min to generate HKCM suspension. Effectiveness of heatkilling was confirmed by plating it on Tryptic Soy Agar with 5% sheep blood plates.

Anti-microbial assay—*C. mastitidis* was prepared as above. Cells were washed twice with 10 mM phosphate buffer, centrifuged at 5,000 rpm for 5 min and suspended in the same buffer to adjust the density to $1x10^5$ to $1x10^6$ CFU/ml. *C. mastitidis* were incubated in triplicate for 3h at 30°C with different concentrations (0, 2 μg/ml, 20 μg/ml, or 100 μg/ml) of mBD-6 (Cusabio), hBD-1 and hBD-3 (Peptides International) in 50 μl of buffers in 96 well round bottom tissue culture plates (Corning). After incubation, 10-fold serial dilutions of the culture suspensions were prepared and 10 ul of each were plated in triplicate on BHI agar plates and incubated for 48h at 37°C. CFU count with β-defensin divided by those without defensin (x 100) represented the percentage of bacterial survival (% live), reflecting the bactericidal activities of the β-defensins.

***C. mastitidis* inoculation—**1×10^8 colony forming units (CFU) of *C. mastitidis* resuspended in BHI medium was applied onto the chest area for 5 consecutive days. BHI medium was applied to control mice.

Mouse keratinocyte culture—MPEK-BL6 cells (Zen-Bio) or $CD45^-EpCAM^+CD200^+CD34^-$ upper HF keratinocytes sorted from 4-week-old C57BL/6 mice were seeded at $3x10^4$ cells/well into Collagen l coated 24 or 48 well plate (Corning) respectively. Cells were cultured in 500 μl of defined PCT Epidermal Keratinocyte Medium (Zen-Bio) at 37°C, 5% CO_2 with a cocktail of ILC-derived cytokines (IL-5, IL-13, IL-17, amphiregulin and bone morphogenetic protein 2) at 100ng/μl concentrations and 50μl of HKCM suspension for 24 to 48 hours. To inhibit caspase-4/11, MPEK-BL6 cells were treated with Caspase-4 Inhibitor Z-YVAD-FMK at 20 to 80 μM concentrations. Acquisition of cell culture images were obtained with ZOE Fluorescent Cell Imager (Bio-Rad).

siRNA knockdown—siRNA transfection was performed one day after seeding keratinocytes with siRNA (ON-TARGETplus SMARTpool, Dharmacon), Lipofectamine RNAiMAX Transfection Reagent (Invitrogen) and Opti-MEM (GIBCO). The optimal concentration for each siRNA was pre-determined individually. Sorted keratinocytes were transfected with siRNA targeting *Adam10* (10nM). MPEK-BL6 cells were transfected with siRNA targeting *Adam10* (30nM), *Rbpj* (50nM), *Myd88* (10nM), *Tlr2* (10nM) and *Tlr5* (50nM) respectively.

Real-time PCR analysis—Total RNA was extracted from sorted mouse keratinocytes or culture keratinocytes using the RNeasy Plus Micro kit (QIAGEN). SuperScript™ IV VILO™ Master Mix with ezDNase™ Enzyme (Thermo Fisher Scientific) was used to synthesize cDNA from mRNA. Real-time PCR analysis was performed using the SYBR™ Green sequence detection system. An Assays-on-Demand gene expression kit (Applied Biosystems) was used for detecting the expression of *Adam10, Defb6, Rbpj, Myd88, Tlr2, Tlr5, Casp1*, and *Casp4*. All samples were normalized to the signal generated from Ribosomal Protein Lateral Stalk Subunit P0 (*Rplp0*).

IL-1 and IL-18 secretion assay—Cell culture supernatants were collected by centrifugation at 2,000 g for 10 min. IL-1α, IL-1β and IL-18 were measured by enzyme-linked immunosorbent assay (ELISA) using a commercial kit (Abcam) as manufacturer

protocols. The intensity of the color was measured with Multimode Plate Reader Victor™ X3 (PerkinElmer).

Enzyme-linked immunosorbent assay for CCL20—0.1g of minced skin was homogenized in 1.5 mL eppendorf tube with tungsten carbide beads (Qiagen) and 300ul lysis buffer using TissueLyser LT (Qiagen). Protein lysates were prepared using RIPA buffer (Cell Signaling Technology) supplemented with protein inhibitor cocktail (Cell Signaling Technology). The homogenates were centrifuged at 13,000 rpm for 10 minutes at 4°C. CCL20 production from skin and serum were determined using Mouse MIP3 alpha ELISA Kit (CCL20) (abcam) respectively.

Hematoxylin and Eosin (H&E) and special stains—Skin samples were harvested from mouse chest skin and were fixed in 10% formalin at room temperature (RT). Samples were then sent to Histoserv, Inc (Germantown, MD), where preparation of paraffin embedded tissue sections and H&E, Gram, Masson Trichrome staining and TUNEL labeling were performed according to standard protocols. Images were captured using a Leica Biosystems microscope or Leica DM2000 microscope (Leica).

Immunohistochemical staining—Skin samples were harvested from mouse chest skin and were fixed in 10% formalin at RT. Samples were then sent to Histoserv, Inc (Germantown, MD). Slides were deparaffinized and hydrated through graded alcohols to distilled water, followed by antigen retrieval. They were then blocked with hydrogen peroxide and a blocking serum (slides were washed in distilled water.) Next, the slides were incubated with the primary antibody, a secondary antibody, and HRP-conjugated Streptavidin. Finally, the slides were developed using DAB and counterstained with Hematoxylin. All incubations were carried at RT and TBST was used as a washing buffer. The anti-gasdermin A antibody is expected to cross-react with gasdermin A3 based on sequence homology.

Immunofluorescent staining—Skin samples were harvested from mouse chest skin and were fixed in acetone for 5 minutes at −20°C or in 4% paraformaldehyde (Thermo Fisher Scientific) in PBS for 15 minutes at RT and were rehydrated or washed in PBS for 5 minutes. They were blocked in 3% dry milk (Sigma) in PBS with 5% goat serum and anti-mouse CD16/32 antibody to block Fc receptors for at least an hour at RT. Primary antibodies conjugated with fluorochromes were diluted in blocking buffer and incubated overnight at 4°C. After washing, sections were mounted with Prolong Gold with DAPI (Thermo Fisher Scientific). For Caspase-11/Caspase-4 staining, sections were blocked in 3% dry milk in PBS with 5% goat serum, washed in PBS, and then incubated overnight at 4°C with an anti-caspase 4 antibody diluted in blocking buffer. Primary antibody was detected with goat anti-rat polyclonal antibody conjugated with AlexaFluor 568 (abcam). Images were observed with Zeiss Axio Observer. Z1 (Carl Zeiss) and collected with the Axiovision software (ver. 4.8). Adjustments of signal levels, if needed, were performed on Photoshop CC 2019 (Adobe) or ImageJ software (version 1.52K), where controls were also treated identically.

Crystal violet staining—Plucked hairs from WT and ADAM10$^{\Delta Mx1}$ mice were fixed in methanol for 10 minutes at −20°C. After air drying, hairs were incubated in 0.5% crystal violet solution (Sigma) in 25% methanol for 10 minutes at RT.

Propidium iodide staining—Plucked hairs from WT and ADAM10$^{\Delta Mx1}$ mice were fixed in acetone for 5 minutes at −20°C. After washing with PBS, hairs were stained with LIVE/DEAD™ *Bac*Light™ Bacterial Viability Kit (Thermo Fisher Scientific) in accordance with the manufacturer protocol.

Hair loss area quantification—The frontal neck to upper chest area was monitored to quantify the hair loss areas. On each mouse image, a trapezoid area connecting bilateral oral angles and axillae were defined as denominator and hair loss area was manually depicted as numerator using the ImageJ software (version 1.52K).

Bulk RNA sequencing—Upper HF and bulge cells were sorted from Rosa26YFP$^{\Delta Mx1}$ or ADAM10;ROSA26YFP$^{\Delta Mx1}$ mice 4 days post-induction with poly(I:C). Epidermal cell suspensions were sorted for viable cells based on SYTOX™Red dead cell stain (Thermo Fisher Scientific). Of the CD45^{-}EpCAM^{+}CD200^{+} HF gate, CD34^{-} infundibulum and isthmus were sorted for YFP^{+} cells and the whole CD34^{+} bulge population, in which YFP expression is not induced, were sorted directly into TRIzol™ Reagent (Life Technologies) using FACS ARIA ll (BD Biosciences). To determine immediate effects of poly(I:C), WT mice were treated once with poly(I:C) injection and the infundibulum and isthmus were sorted 24hrs after. Total RNA was extracted using Direct-zol RNA MicroPrep (Zymo Research). RNA libraries were prepared using a NEBNext Poly(A) mRNA Magnetic Isolation Module (New England BioLabs), NEBNext Ultra RNA Library Prep Kit for Illumina (New England BioLabs) and NEBNext Multiplex Oligos for Illumina (Index Primers Set) (New England BioLabs) according to manufacturer protocol. The libraries were sequenced for 50 cycles (single read) using the Hiseq3000 (Illumina). The FASTQ files were aligned to the reference mouse genome (mm10) using STAR software (2.6.1c). Gene-level count matrix was generated from mapped reads via GenomicFeatures and GenomicAlignments tools on R platform and then used as an input for downstream analysis using DESeq2 or kallisto (ver. 0.44.0), a pseudoalignment tool and sleuth pipeline (Bray et al., 2016). Genes with lower than 10 read count were filtered out from further analysis. The differentially expressed genes were based on a threshold of false discovery rate below 0.1. Unsupervised heatmaps were generated using differentially expressed genes with further selection criteria on p-value (<0.05) and fold change (−1<Log2 and Log2>1) and graphed with pheatmap package in R. Pathway analysis was performed with Database for Annotation Visualization and Integrated Discovery (DAVID) v6.8 (https://david.ncifcrf.gov).

Single-cell RNA sequencing—CD45^{-} non-immune cells or CD45+ immune cells were sorted from WT, ADAM10$^{\Delta Mx1}$, ADAM10$^{\Delta Mx1}$ *Rag2*$^{-/-}$, RBPJ$^{\Delta Mx1}$ mice 30 days post-induction with poly(I:C). Whole skin cell suspensions were sorted for viable cells based on SYTOXTMRed dead cell stain. Cells were further sorted into CD45^{-} or CD45+ cells using FACS ARIA ll (BD Biosciences). Droplet-based scRNA-seq captures were performed with 10x Chromium (10x Genomics) in accordance with the manufacturer

protocol. cDNA libraries were prepared following the recommended protocol for the Chromium Single Cell 3' Reagent Kit (v2 Chemistry for main figure datasets, v3 Chemistry for supplementary figure datasets). Sequencing was performed with HiSeq3000 sequencer (Illumina). Post-processing and quality control were performed using the 10x Cell Ranger pipelines (v2.2.0 for main figure datasets, v3.0.2 for supplementary figure datasets, 10x Genomics). Reads were aligned to mouse reference genome (mm10) using a STAR aligner to produce the digital gene expression matrix (10x Genomics Cell Ranger). Seurat R package (Butler et al., 2018) was used for further analysis with default parameters applied unless otherwise indicated. Quality control metrics excluded cells with >8% mitochondrial gene load, <300 total genes, >4300 to 4750 total genes, and >21000 to 28000 UMI/cell count depending on the datasets. Each sample was then Log normalized (NormalizeData function) and Scaled (ScaleData function, including a linear regression of 'mitochondrial gene percentage' to reduce these sources of variation). Top 2000 highly variable genes were used for canonical correlation analysis (CCA) implemented in Seurat to align samples using 16 CCs. Cell clustering was performed by 'FindClusters' function and dimensionality reduction was performed with 'RunTSNE' or 'RunUMAP'. DEGs were obtained using function 'FindMarkers' calculated by using the non-parametric two-sided Wilcoxon rank sum test in Seurat and filtered with adjusted p-values <0.05. Log-normalized gene expression count was used for visualizations of projected gene expression on dimensionality reduction plot using 'FeaturePlot' function. Violin plots were generated by ggplot2 package using log-normalized gene expression value. Gene sets enrichment score analysis using 'AddModuleScore' function in Seurat, using indicated gene set list. Heatmaps were created with 'DoHeatmap' function in Seurat. Pathway analysis was performed by Metascape (http://metascape.org/).

Western blot analysis—Epidermal cell keratinocytes were isolated from WT and ADAM10$^{\Delta Mx1}$ mice 30 days post-induction with poly(I:C) via CD45 MicroBeads and auto MACS pro. Protein lysates were prepared using RIPA buffer (Cell Signaling Technology) supplemented with protein inhibitor cocktail (Cell Signaling Technology). Following centrifugation, cell lysates were dissolved in 4x sample buffer (Invitrogen) containing NuPAGE sample reducing agent (Invitrogen) and boiled at 95°C for 5min. A total of 20 ug lysates were separated by electrophoresis (4-20% SDS PAGE, Bio-Rad) and transferred on PVDF membranes (Bio-Rad) using Trans-Blot Turbo transfer system (Bio-Rad). Proteins were blotted with a rat anti-Caspase 11/4 antibody (Invitrogen), mouse anti-Caspase 1 antibody (Invitrogen), rabbit anti-GSDMC (Proteintech), rabbit anti-GSDMA (LS Bio), and HRP-conjugated Vinculin (Santa Cruz) antibodies. The anti-GSDMA antibody is expected to cross-react with gasdermin A3 based on sequence homology. Membrane was then incubated with goat anti-rabbit, -mouse or -rat IgG-HRP conjugates (Jackson Immuno Research) secondary antibodies. Following three washing with TBST (Thermo Fisher Scientific), membrane was developed by using Pierce ECL Western blotting substrate (Thermo Fisher Scientific) and images were acquired using a ChemiDoc Touch Image System (Bio-Rad). Protein loading was normalized against vinculin.

DNA extraction, PCR amplification and sequencing for microbiome analysis—Swab samples using sterile foam swabs (Puritan, 25-1506 1PF) were collected from the

face, neck and chest area of mice and processed as described previously. Briefly, skin swabs using sterile foam swabs were collected after pre-moistening with 100 ul of Yeast Cell Lysis Buffer (Lucigen) aliquoted in 2.0 ml tubes (Eppendorf, 4060-0044). Control swabs to monitor for potential contamination were obtained by exposing pre-moistened swabs to environmental air. Swabs were stored in 2.0 ml tubes at −80°C following collection. For DNA extraction, swabs were incubated in Yeast Cell Lysis buffer and ReadyLyse Lysozyme Solution (Lucigen) for 3hrs with shaking at 37°C, followed by 5-mm steel bead-beating using a Tissuelyser (QIAGEN) for 2 min at 30 Hz, and 1hr incubation at 65°C for complete lysis. MPC Reagent was then added and centrifuged to samples to remove cellular debris and proteins. Resulting supernatant was processed using the PureLink Genomic DNA Kit (Invitrogen). DNA was eluted in DNA-Free PCR Water (MoBio). Control swabs also underwent the same DNA extraction processes and sequencing along with experimental samples, and no apparent contamination from either reagents or experimental procedures were observed. The V1-V3 region was amplified using primers 27F (5'-AGAGTTTGATCCTGGCTCAG) and 534R (5'-ATTACCGCGGCTGCTGG) with Illumina adapters. PCR reactions were performed in duplicate for 30 cycles, combined, purified using Agencourt AmpureXP (Beckman Coulter), and quantified using the Quant-IT dsDNA Kit (Invitrogen). Equivalent amounts of amplicons were pooled together, purified (MinElute PCR Purification Kit; QIAGEN), and sequenced on an Illumina MiSeq platform.

Microbiome analysis pipeline—For sequence analysis, a mothur-based pipeline was used (Kobayashi et al., 2019; Kong et al., 2012; Schloss et al., 2009). Briefly, sequences were pre-processed to remove primers and barcodes, and paired-end reads were merged using FLASh. Assembled reads were quality filtered (qaverage=25), subsampled to 5000 sequences per sample, and checked for chimeras using UCHIME in mothur (Edgar et al., 2011). After chimeras were removed, reads were clustered into operational taxonomic units (OTUs) at 97% nucleotide similarity (average neighbor). Each OTU classified down to genus-level using RDP database (Cole et al., 2014).

QUANTIFICATION AND STATISTICAL ANALYSIS

Statistical analysis—Quantitative data were visualized and analyzed using GraphPad Prism software. Student's *t* test was used to measure significance between two groups and ANOVA with Tukey's multiple comparison test was used to measure significance when comparing multiple groups. Significance is indicated as follows in all figures: ns = not significant, *$p < 0.05$, **$p < 0.01$, ***$p < 0.001$, ****$p < 0.0001$. Number of mice in each group is indicated in figure legends for main figures, and in the figure for Supplemental figures. Replicate number for each in vitro experiment is in the figure legend. All error bars represent mean ± standard deviation.

Supplementary Material

Refer to Web version on PubMed Central for supplementary material.

Acknowledgments:

Authors thank Genome Analysis Core Facility, Flow Cytometry Section, Light Imaging Section, and H. Nagashima (NIAMS); and T. Nakatsuji (UC San Diego) for their technical support and advice. This work was supported by the Intramural Research Programs of NIAMS and NHGRI.

References

Abu Khweek A, and Amer AO (2020). Pyroptotic and non-pyroptotic effector functions of caspase-11. Immunol. Rev 297, e12910.

Adachi T, Kobayashi T, Sugihara E, Yamada T, Ikuta K, Pittaluga S, Saya H, Amagai M, and Nagao K (2015). Hair follicle-derived IL-7 and IL-15 mediate skin-resident memory T cell homeostasis and lymphoma. Nat. Med 21, 1272–1279. [PubMed: 26479922]

Adler BL, and Christopher-Stine L (2018). Triggers of inflammatory myopathy: insights into pathogenesis. Discov Med 25, 75–83. [PubMed: 29579414]

Ali RS, Falconer A, Ikram M, Bissett CE, Cerio R, and Quinn AG (2001). Expression of the peptide antibiotics human beta defensin-1 and human beta defensin-2 in normal human skin. J. Invest. Dermatol 117, 106–111. [PubMed: 11442756]

Almazán-Fernández FM, and Fernández-Crehuet Serrano P (2017). Trichomycosis axillaris dermoscopy. Dermatol. Online J 23.

Anzai A, Wang EHC, Lee EY, Aoki V, and Christiano AM (2019). Pathomechanisms of immune-mediated alopecia. Int. Immunol 31, 439–447. [PubMed: 31050755]

Barreiro O, Cibrian D, Clemente C, Alvarez D, Moreno V, Valiente Í, Bernad A, Vestweber D, Arroyo AG, Martín P, et al. (2016). Pivotal role for skin transendothelial radio-resistant anti-inflammatory macrophages in tissue repair. eLife 5, e15251. [PubMed: 27304075]

Belkaid Y, and Segre JA (2014). Dialogue between skin microbiota and immunity. Science 346, 954. [PubMed: 25414304]

Bray NL, Pimentel H, Melsted P, and Pachter L (2016). Near-optimal probabilistic RNA-seq quantification. Nat Biotechnol 34, 525–527. [PubMed: 27043002]

Casson CN, Copenhaver AM, Zwack EE, Nguyen HT, Strowig T, Javdan B, Bradley WP, Fung TC, Flavell RA, Brodsky IE, et al. (2013). Caspase-11 activation in response to bacterial secretion systems that access the host cytosol. PLoS Pathog. 9, e1003400. [PubMed: 23762026]

Chessa C, Bodet C, Jousselin C, Wehbe M, Lévêque N, and Garcia M (2020). Antiviral and Immunomodulatory Properties of Antimicrobial Peptides Produced by Human Keratinocytes. Frontiers in microbiology 11, 1155–1155. [PubMed: 32582097]

Cobo ER, and Chadee K (2013). Antimicrobial Human β-Defensins in the Colon and Their Role in Infectious and Non-Infectious Diseases. Pathogens (Basel, Switzerland) 2, 177–192.

Cole JR, Wang Q, Fish JA, Chai B, McGarrell DM, Sun Y, Brown CT, Porras-Alfaro A, Kuske CR, and Tiedje JM (2014). Ribosomal Database Project: data and tools for high throughput rRNA analysis. Nucleic Acids Res. 42, D633–642. [PubMed: 24288368]

Cotsarelis G, Sun TT, and Lavker RM (1990). Label-retaining cells reside in the bulge area of pilosebaceous unit: implications for follicular stem cells, hair cycle, and skin carcinogenesis. Cell 61, 1329–1337. [PubMed: 2364430]

Di Domizio J, Belkhodja C, Chenuet P, Fries A, Murray T, Mondéjar PM, Demaria O, Conrad C, Homey B, Werner S, et al. (2020). The commensal skin microbiota triggers type I IFN–dependent innate repair responses in injured skin. Nat. Immunol 21, 1034–1045. [PubMed: 32661363]

Dickensheets H, Sheikh F, Park O, Gao B, and Donnelly RP (2013). Interferon-lambda (IFN-λ) induces signal transduction and gene expression in human hepatocytes, but not in lymphocytes or monocytes. J. Leukoc. Biol 93, 377–385. [PubMed: 23258595]

Edgar RC, Haas BJ, Clemente JC, Quince C, and Knight R (2011). UCHIME improves sensitivity and speed of chimera detection. Bioinformatics 27, 2194–2200. [PubMed: 21700674]

Edwards DR, Handsley MM, and Pennington CJ (2008). The ADAM metalloproteinases. Mol. Asp. Med 29, 258–289.

Filippi CM, and von Herrath MG (2008). Viral Trigger for Type 1 Diabetes. Diabetes 57, 2863. [PubMed: 18971433]

Flamm A, Moshiri AS, Roche F, Onyekaba G, Nguyen J, James AJ, Taylor S, and Seykora JT (2020). Characterization of the inflammatory features of central centrifugal cicatricial alopecia. J. Cutan. Pathol 47, 530–534. [PubMed: 32068905]

Geoghegan JA, Irvine AD, and Foster TJ (2018). Staphylococcus aureus and Atopic Dermatitis: A Complex and Evolving Relationship. Trends Microbiol 26, 484–497. [PubMed: 29233606]

Gonzales KAU, and Fuchs E (2017). Skin and Its Regenerative Powers: An Alliance between Stem Cells and Their Niche. Dev. Cell 43, 387–401. [PubMed: 29161590]

Harder J, Bartels J, Christophers E, and Schroder JM (2001). Isolation and characterization of human beta -defensin-3, a novel human inducible peptide antibiotic. J. Biol. Chem 276, 5707–5713. [PubMed: 11085990]

Harries MJ, and Paus R (2010). The pathogenesis of primary cicatricial alopecias. Am. J. Pathol 177, 2152–2162. [PubMed: 20889564]

Harrison OJ, Linehan JL, Shih HY, Bouladoux N, Han SJ, Smelkinson M, Sen SK, Byrd AL, Enamorado M, Yao C, et al. (2019). Commensal-specific T cell plasticity promotes rapid tissue adaptation to injury. Science 363.

Hartmann D, de Strooper B, Serneels L, Craessaerts K, Herreman A, Annaert W, Umans L, Lubke T, Lena Illert A, von Figura K, et al. (2002). The disintegrin/metalloprotease ADAM 10 is essential for Notch signalling but not for alpha-secretase activity in fibroblasts. Hum. Mol. Genet 11, 2615–2624. [PubMed: 12354787]

Hou J, Zhao R, Xia W, Chang C-W, You Y, Hsu J-M, Nie L, Chen Y, Wang Y-C, Liu C, et al. (2020). PD-L1-mediated gasdermin C expression switches apoptosis to pyroptosis in cancer cells and facilitates tumour necrosis. Nat. Cell Biol 22, 1264–1275. [PubMed: 32929201]

Huang Y, Guo L, Qiu J, Chen X, Hu-Li J, Siebenlist U, Williamson PR, Urban JF Jr., and Paul WE (2015). IL-25-responsive, lineage-negative KLRG1(hi) cells are multipotential 'inflammatory' type 2 innate lymphoid cells. Nat. Immunol 16, 161–169. [PubMed: 25531830]

Huang Y, Mao K, Chen X, Sun MA, Kawabe T, Li W, Usher N, Zhu J, Urban JF Jr., Paul WE, et al. (2018). S1P-dependent interorgan trafficking of group 2 innate lymphoid cells supports host defense. Science 359, 114–119. [PubMed: 29302015]

Illescas-Montes R, Corona-Castro CC, Melguizo-Rodríguez L, Ruiz C, and Costela-Ruiz VJ (2019). Infectious processes and systemic lupus erythematosus. Immunology 158, 153–160. [PubMed: 31386190]

Ito T, and Tokura Y (2012). Alopecia areata triggered or exacerbated by swine flu virus infection. J Dermatol 39, 863–864. [PubMed: 22142460]

Joost S, Zeisel A, Jacob T, Sun X, La Manno G, Lönnerberg P, Linnarsson S, and Kasper M (2016). Single-Cell Transcriptomics Reveals that Differentiation and Spatial Signatures Shape Epidermal and Hair Follicle Heterogeneity. Cell Syst. 3, 221–237.e229. [PubMed: 27641957]

Joshi SS, Tandukar B, Pan L, Huang JM, Livak F, Smith BJ, Hodges T, Mahurkar AA, and Hornyak TJ (2019). CD34 defines melanocyte stem cell subpopulations with distinct regenerative properties. PLoS Genet. 15, e1008034–e1008034. [PubMed: 31017901]

Kesavardhana S, Malireddi RKS, and Kanneganti T-D (2020). Caspases in Cell Death, Inflammation, and Pyroptosis. Annu. Revi. Immunol 38, 567–595.

Klotman ME, and Chang TL (2006). Defensins in innate antiviral immunity. Nat Rev Immunol 6, 447–456. [PubMed: 16724099]

Kobayashi T, Glatz M, Horiuchi K, Kawasaki H, Akiyama H, Kaplan DH, Kong HH, Amagai M, and Nagao K (2015). Dysbiosis and Staphylococcus aureus Colonization Drives Inflammation in Atopic Dermatitis. Immunity 42, 756–766. [PubMed: 25902485]

Kobayashi T, Voisin B, Kim DY, Kennedy EA, Jo JH, Shih HY, Truong A, Doebel T, Sakamoto K, Cui CY, et al. (2019). Homeostatic Control of Sebaceous Glands by Innate Lymphoid Cells Regulates Commensal Bacteria Equilibrium. Cell 176, 982–997.e916. [PubMed: 30712873]

Kong HH, Oh J, Deming C, Conlan S, Grice EA, Beatson MA, Nomicos E, Polley EC, Komarow HD, Murray PR, et al. (2012). Temporal shifts in the skin microbiome associated with disease flares and treatment in children with atopic dermatitis. Genome Res. 22, 850–859. [PubMed: 22310478]

Kubo A, Nagao K, and Amagai M (2012). Epidermal barrier dysfunction and cutaneous sensitization in atopic diseases. J Clin Invest 122, 440–447. [PubMed: 22293182]

Kühn R, Schwenk F, Aguet M, and Rajewsky K (1995). Inducible gene targeting in mice. Science. 269, 1427–1429. [PubMed: 7660125]

Linehan JL, Harrison OJ, Han SJ, Byrd AL, Vujkovic-Cvijin I, Villarino AV, Sen SK, Shaik J, Smelkinson M, Tamoutounour S, et al. (2018). Non-classical Immunity Controls Microbiota Impact on Skin Immunity and Tissue Repair. Cell 172, 784–796.e718. [PubMed: 29358051]

Loschko J, Rieke GJ, Schreiber HA, Meredith MM, Yao KH, Guermonprez P, and Nussenzweig MC (2016). Inducible targeting of cDCs and their subsets in vivo. J Immunol Methods 434, 32–38. [PubMed: 27073171]

Manohar P, Loh B, Athira S, Nachimuthu R, Hua X, Welburn SC, and Leptihn S (2020). Secondary Bacterial Infections During Pulmonary Viral Disease: Phage Therapeutics as Alternatives to Antibiotics? Frontiers in Microbiology 11.

McNab F, Mayer-Barber K, Sher A, Wack A, and O'Garra A (2015). Type I interferons in infectious disease. Nat Rev Immunol 15, 87–103. [PubMed: 25614319]

Meade KG, and O'Farrelly C (2019). β-Defensins: Farming the Microbiome for Homeostasis and Health. Frontiers in Immunology 9.

Melo-Gonzalez F, and Hepworth MR (2017). Functional and phenotypic heterogeneity of group 3 innate lymphoid cells. Immunology 150, 265–275. [PubMed: 27935637]

Merad M, Manz MG, Karsunky H, Wagers A, Peters W, Charo I, Weissman IL, Cyster JG, and Engleman EG (2002). Langerhans cells renew in the skin throughout life under steady-state conditions. Nat Immunol 3, 1135–1141. [PubMed: 12415265]

Morris RJ, Liu Y, Marles L, Yang Z, Trempus C, Li S, Lin JS, Sawicki JA, and Cotsarelis G (2004). Capturing and profiling adult hair follicle stem cells. Nat. Biotechnol 22, 411–417. [PubMed: 15024388]

Murtaugh LC, Stanger BZ, Kwan KM, and Melton DA (2003). Notch signaling controls multiple steps of pancreatic differentiation. Proc. Natl. Acad. Sci. U.S.A 100, 14920–14925. [PubMed: 14657333]

Nagao K, Kobayashi T, Moro K, Ohyama M, Adachi T, Kitashima DY, Ueha S, Horiuchi K, Tanizaki H, Kabashima K, et al. (2012). Stress-induced production of chemokines by hair follicles regulates the trafficking of dendritic cells in skin. Nat. Immunol 13, 744–752. [PubMed: 22729248]

Naik S, Bouladoux N, Linehan JL, Han SJ, Harrison OJ, Wilhelm C, Conlan S, Himmelfarb S, Byrd AL, Deming C, et al. (2015). Commensal-dendritic-cell interaction specifies a unique protective skin immune signature. Nature 520, 104–108. [PubMed: 25539086]

Nishimura EK, Jordan SA, Oshima H, Yoshida H, Osawa M, Moriyama M, Jackson IJ, Barrandon Y, Miyachi Y, and Nishikawa S (2002). Dominant role of the niche in melanocyte stem-cell fate determination. Nature 416, 854–860. [PubMed: 11976685]

Peschon JJ, Morrissey PJ, Grabstein KH, Ramsdell FJ, Maraskovsky E, Gliniak BC, Park LS, Ziegler SF, Williams DE, Ware CB, et al. (1994). Early lymphocyte expansion is severely impaired in interleukin 7 receptor-deficient mice. J. Exp. Med 180, 1955–1960. [PubMed: 7964471]

Rodriguez TA, and Duvic M (2008). Onset of alopecia areata after Epstein-Barr virus infectious mononucleosis. J Am Acad Dermatol 59, 137–139. [PubMed: 18329131]

Rosenblum MD, Olasz EB, Yancey KB, Woodliff JE, Lazarova Z, Gerber KA, and Truitt RL (2004). Expression of CD200 on epithelial cells of the murine hair follicle: a role in tissue-specific immune tolerance? J. Invest. Dermatol 123, 880–887. [PubMed: 15482475]

Schloss PD, Westcott SL, Ryabin T, Hall JR, Hartmann M, Hollister EB, Lesniewski RA, Oakley BB, Parks DH, Robinson CJ, et al. (2009). Introducing mothur: open-source, platform-independent, community-supported software for describing and comparing microbial communities. Appl. Environ. Microbiol 75, 7537–7541. [PubMed: 19801464]

Semple CA, Maxwell A, Gautier P, Kilanowski FM, Eastwood H, Barran PE, and Dorin JR (2005). The complexity of selection at the major primate beta-defensin locus. BMC Evol Biol 5, 32. [PubMed: 15904491]

Sheikh A, and Abraham N (2019). Interleukin-7 Receptor Alpha in Innate Lymphoid Cells: More Than a Marker. Front. Immunol 10, 2897. [PubMed: 31921158]

Shi J, Zhao Y, Wang Y, Gao W, Ding J, Li P, Hu L, and Shao F (2014). Inflammatory caspases are innate immune receptors for intracellular LPS. Nature 514, 187–192. [PubMed: 25119034]

Silva P, Gonçalves S, and Santos N (2014). Defensins: antifungal lessons from eukaryotes. Frontiers in Microbiology 5.

Takeuchi O, and Akira S (2010). Pattern Recognition Receptors and Inflammation. Cell 140, 805–820. [PubMed: 20303872]

Tanigaki K, Han H, Yamamoto N, Tashiro K, Ikegawa M, Kuroda K, Suzuki A, Nakano T, and Honjo T (2002). Notch-RBP-J signaling is involved in cell fate determination of marginal zone B cells. Nat. Immunol 3, 443–450. [PubMed: 11967543]

Veniaminova NA, Vagnozzi AN, Kopinke D, Do TT, Murtaugh LC, Maillard I, Dlugosz AA, Reiter JF, and Wong SY (2013). Keratin 79 identifies a novel population of migratory epithelial cells that initiates hair canal morphogenesis and regeneration. Development 140, 4870. [PubMed: 24198274]

Weber S, Niessen MT, Prox J, Lullmann-Rauch R, Schmitz A, Schwanbeck R, Blobel CP, Jorissen E, de Strooper B, Niessen CM, et al. (2011). The disintegrin/metalloproteinase Adam10 is essential for epidermal integrity and Notch-mediated signaling. Development 138, 495–505. [PubMed: 21205794]

Whiting DA, and Olsen EA (2008). Central centrifugal cicatricial alopecia. Dermatol. Ther 21, 268–278. [PubMed: 18715297]

Wilke GA, and Bubeck Wardenburg J (2010). Role of a disintegrin and metalloprotease 10 in Staphylococcus aureus alpha-hemolysin-mediated cellular injury. Proc. Natl. Acad. Sci. U.S.A 107, 13473–13478. [PubMed: 20624979]

Yamaguchi Y, Nagase T, Makita R, Fukuhara S, Tomita T, Tominaga T, Kurihara H, and Ouchi Y (2002). Identification of multiple novel epididymis-specific beta-defensin isoforms in humans and mice. J. Immunol 169, 2516–2523. [PubMed: 12193721]

Yi B, Dalpke AH, and Boutin S (2021). Changes in the Cystic Fibrosis Airway Microbiome in Response to CFTR Modulator Therapy. Frontiers in cellular and infection microbiology 11, 548613–548613. [PubMed: 33816324]

Yoda M, Kimura T, Tohmonda T, Uchikawa S, Koba T, Takito J, Morioka H, Matsumoto M, Link DC, Chiba K, et al. (2011). Dual functions of cell-autonomous and non-cell-autonomous ADAM10 activity in granulopoiesis. Blood 118, 6939–6942. [PubMed: 22042698]

Zhao L, Wang B, Gomez NA, de Avila JM, Zhu MJ, and Du M (2020). Even a low dose of tamoxifen profoundly induces adipose tissue browning in female mice. Int. J. Obes 44, 226–234.

Highlights

- ADAM10-Notch axis bolsters epithelial innate immunity in IFN-responsive HF cells
- Lack of ADAM10-Notch axis leads to follicular dysbiosis predominated by *C. mastitidis*
- Dysbiosis triggers ILC2-mediated inflammation that depends on IL-7R, S1P1R and CCR6
- HFs undergo pyroptotic cell death, resulting in irreversible alopecia

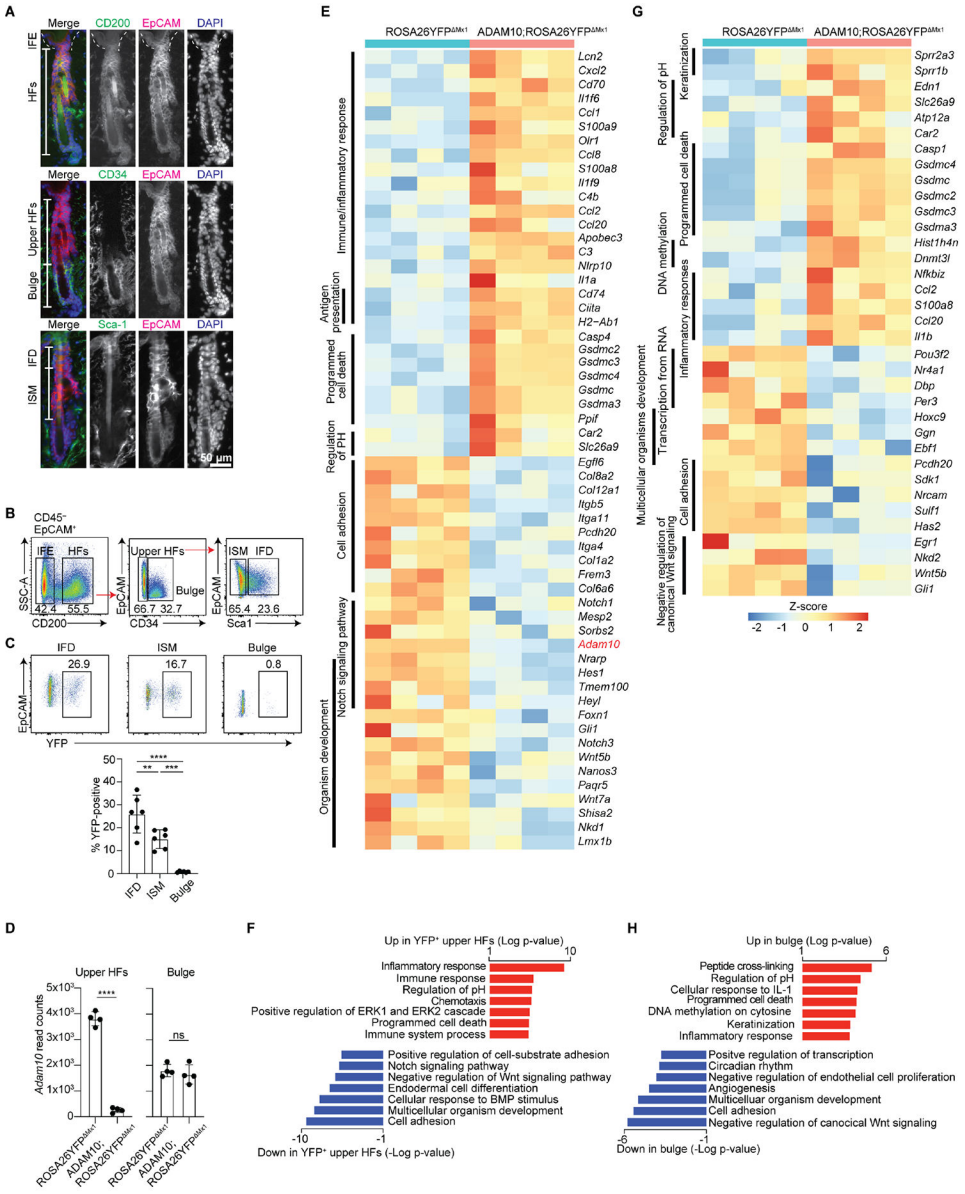

Fig. 1. Ablation of *Adam10* triggers an inflammatory transcriptome.

(A) Representative immunofluorescence microscopy of HF subsets in C57BL/6 mice. (B) Representative flow cytometry and frequencies of bulge, isthmus (ISM), and infundibulum (IFD). (C) Flow cytometry and quantification of YFP expression by HF subsets in ROSA26YFP$^{\Delta Mx1}$ mice (n=6, pooled from two independent experiments). (D) *Adam10* read counts from bulk RNA-seq analysis of sorted uHFs YFP^{+} cells from induced ROSA26YFP$^{\Delta Mx1}$ and ADAM10;ROSA26YFP$^{\Delta Mx1}$ mice (n=4 per group). Heatmaps from RNA-seq analysis for selected DEGs with annotation of associated pathways in (E and F) uHFs and (G and H) in bulge cells. (C–F) Mice were harvested 4 days post-induction.

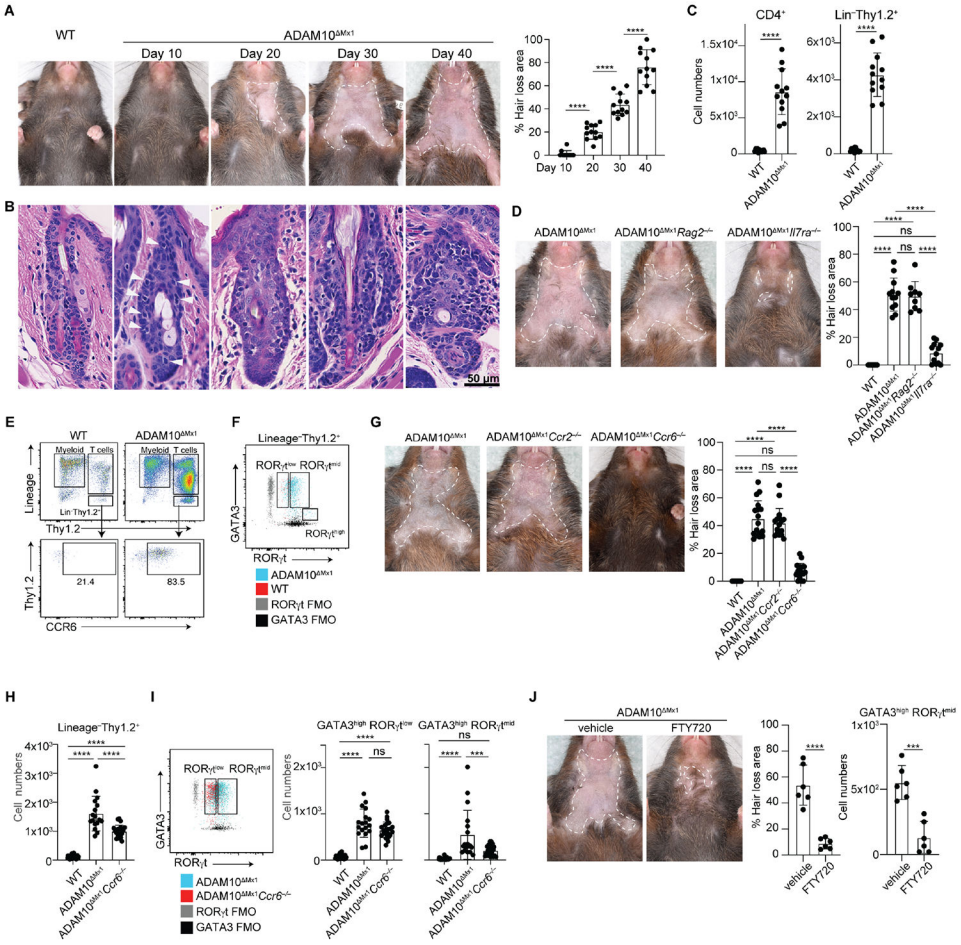

Fig. 2. Inflammatory ILC2s mediates HF destruction.

(A) Hair loss progression in ADAM10$^{\Delta Mx1}$ mice (n=12) and (B) Representative H&E staining of skin sections at indicated days post-induction. Arrowheads depict lymphocytic infiltrates. (C) Quantification of indicated cell types by flow cytometry (n=12 per group). (D) Gross phenotype and hair loss area in indicated mice (n=8–12 per group). (E) Flow cytometry for CCR6 on gated lineage^{-} Thy1^{+} ILC populations. (F) Representative flow cytometry plot of GATA3^{high}RORγt$^{low\text{-}mid}$ ILC2s and GATA3^{low}RORγt^{high} ILC3s in indicated mice. FMO: fluorescence minus one. (G) Gross phenotype and hair loss area in indicated mice (n=17 per group). (H) Quantification of lineage^{-}Thy1^{+} ILC populations in indicated mice. (I) Flow cytometry and quantification of GATA3^{high} RORγt^{mid} and GATA3^{high}RORγt^{low} ILC2 subsets in indicated mice. (n=16–22 per group). (J) Gross phenotype, hair loss area, and GATA3^{high}RORgt^{mid} ILC2 quantification in indicated mice (n=6 per group, pooled from two independent experiments). See also Figure S1 and S2.

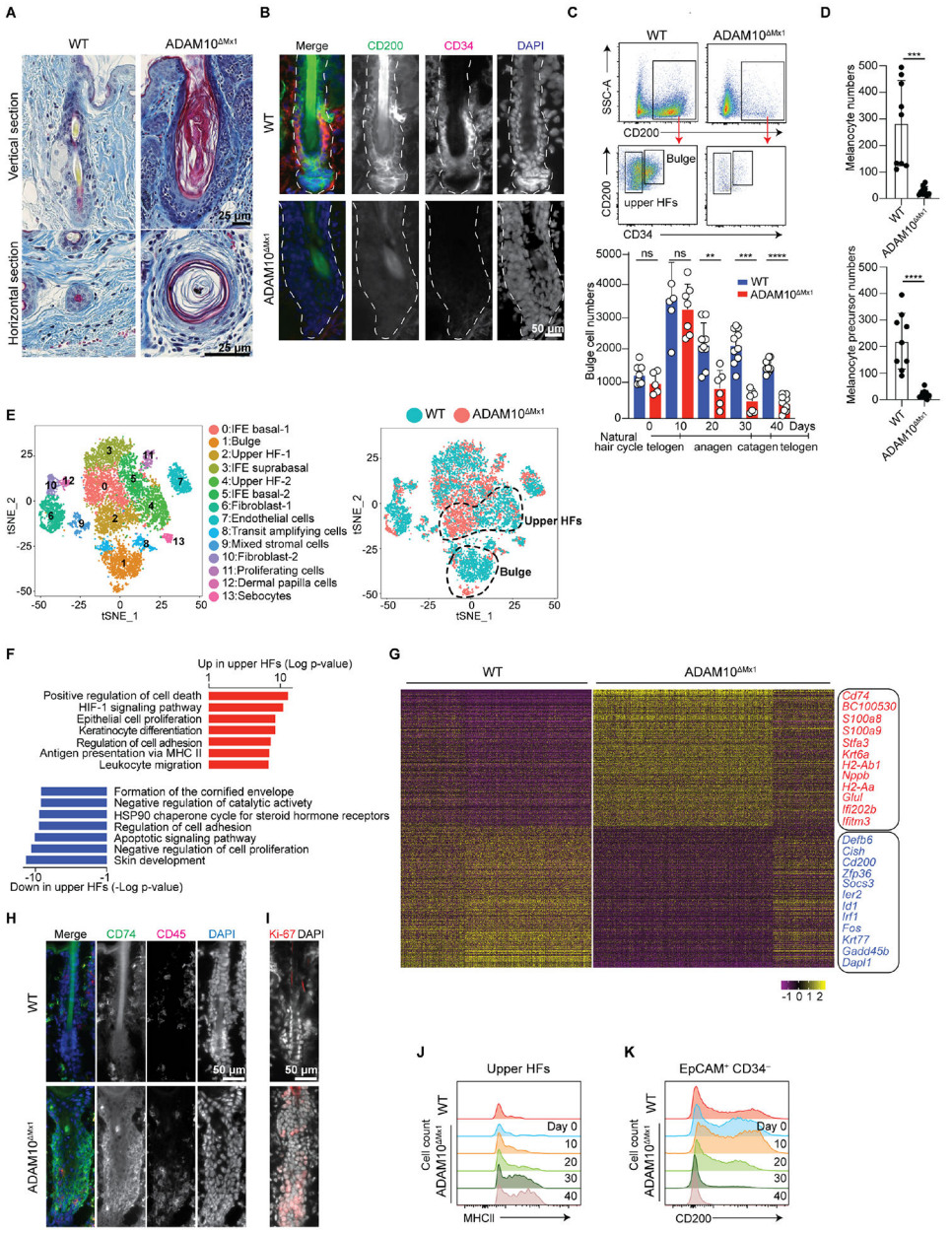

Fig. 3. ADAM10$^{\Delta Mx1}$ mice recapitulate cicatricial alopecia

(A) Representative Masson's trichrome staining of skin sections from indicated mice. (B) Representative immunofluorescence microscopy of the HFs. CD200^{+}CD34^{+} area represents the bulge. (C) Quantification of bulge cell numbers from indicated mice via flow cytometry at indicated time points (n=6–9 per group). (D) Quantification of c-kit^{+} melanocytes and c-kit^{+} CD34^{+} precursor numbers (n=9–10 per group, pooled from two independent experiments). (E) Unsupervised clustering analysis and t-SNE plot (left) from scRNA-seq on CD45^{-} cells sorted from the skin of WT and ADAM10$^{\Delta Mx1}$ mice (pooled from 3 mice in each group), color-coded based on sample origin (right). (F) Pathway analysis of DEGs between uHF clusters 2 and 4, and (G) overview heatmap annotated for selected genes. (H) Immunofluorescence microscopy for CD74 in HFs (CD45^{-}) and (I) Ki-67. (J)

Representative flow cytometry for MHC ll and (K) CD200 in HFs at the indicated time points. (C and D).

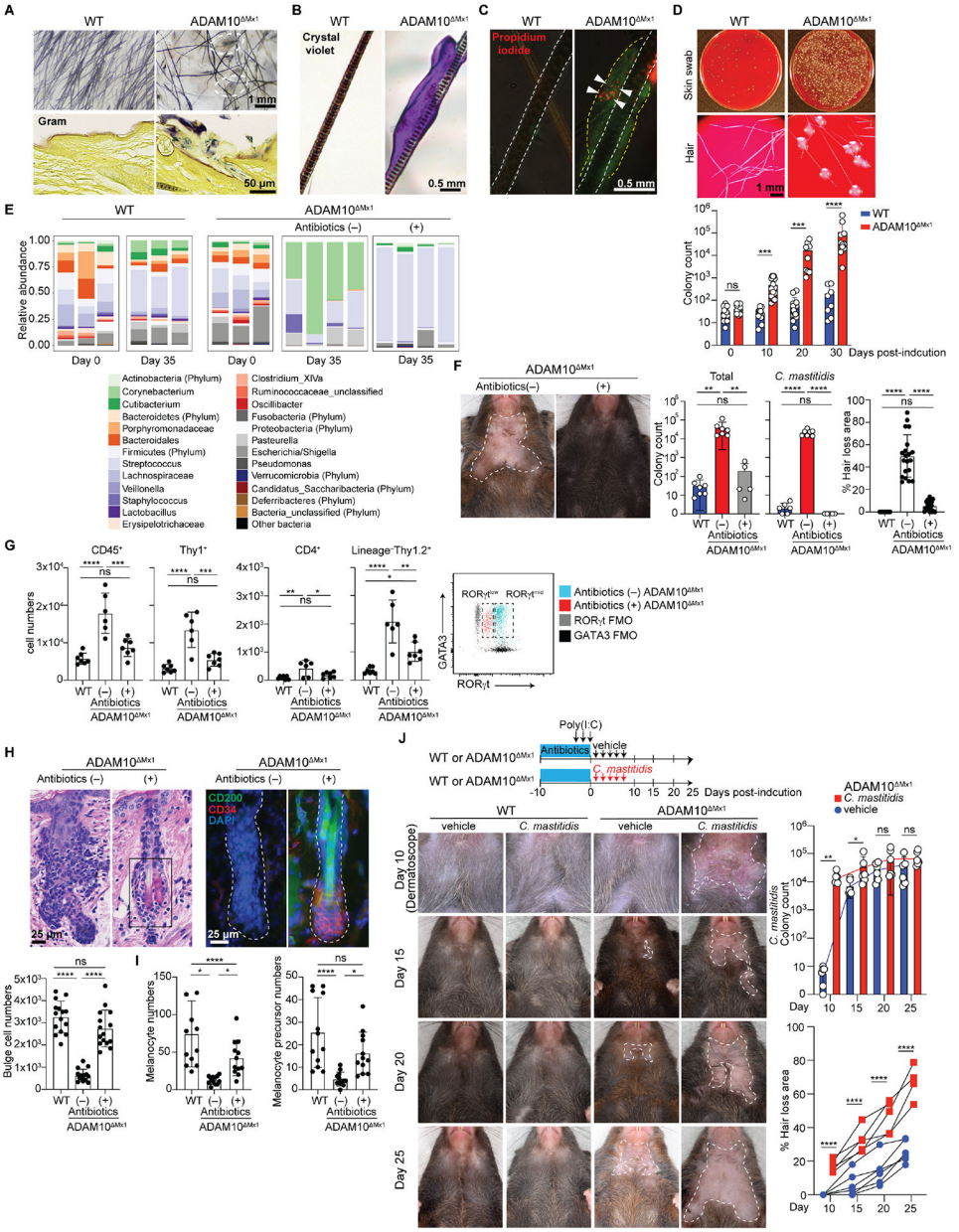

Fig. 4. Dysbiosis triggers inflammatory destruction of HFs

(A) Representative dissecting microscopic images of indicated mouse skin surfaces (upper). Dotted circles depict concretions. Gram stain in uHFs (lower). (B) Representative crystal violet and (C) propidium iodide staining of plucked hairs from indicated mice. Arrowheads depict bacteria-like elements. n=3, two independent experiments. (D) Representative skin swab and hair bacterial cultures. Colony count from skin swab cultures (n=9–15). (E) Relative abundance of major taxa via 16S rRNA sequencing analysis of skin swab samples from WT and ADAM10$^{\Delta Mx1}$ mice with or without antibiotics. Each bar depicts one mouse, n=3-4 from two independent experiments. (F) Gross phenotype, hair loss area (n=20 per group), and total or *C. mastitidis* colony count from skin swab cultures of indicated mice (n=5–7 per group). (G) Quantification of relevant immune cell subsets via flow cytometry

with representative plots for ILC2s in indicated mice. (H) H&E and immunofluorescence microscopy for bulge markers. Rectangle depicts the bulge. Quantification of bulge cells via flow cytometry (n=15 per group). (I) Quantification of melanocytes and its precursors from indicated mice (n=12 per group). (J) Gross phenotype, hair loss area and *C. mastitidis* colony count from skin swab cultures of indicated mice (n=5 per group, representative of two independent experiments). See also Figure S3 and S4.

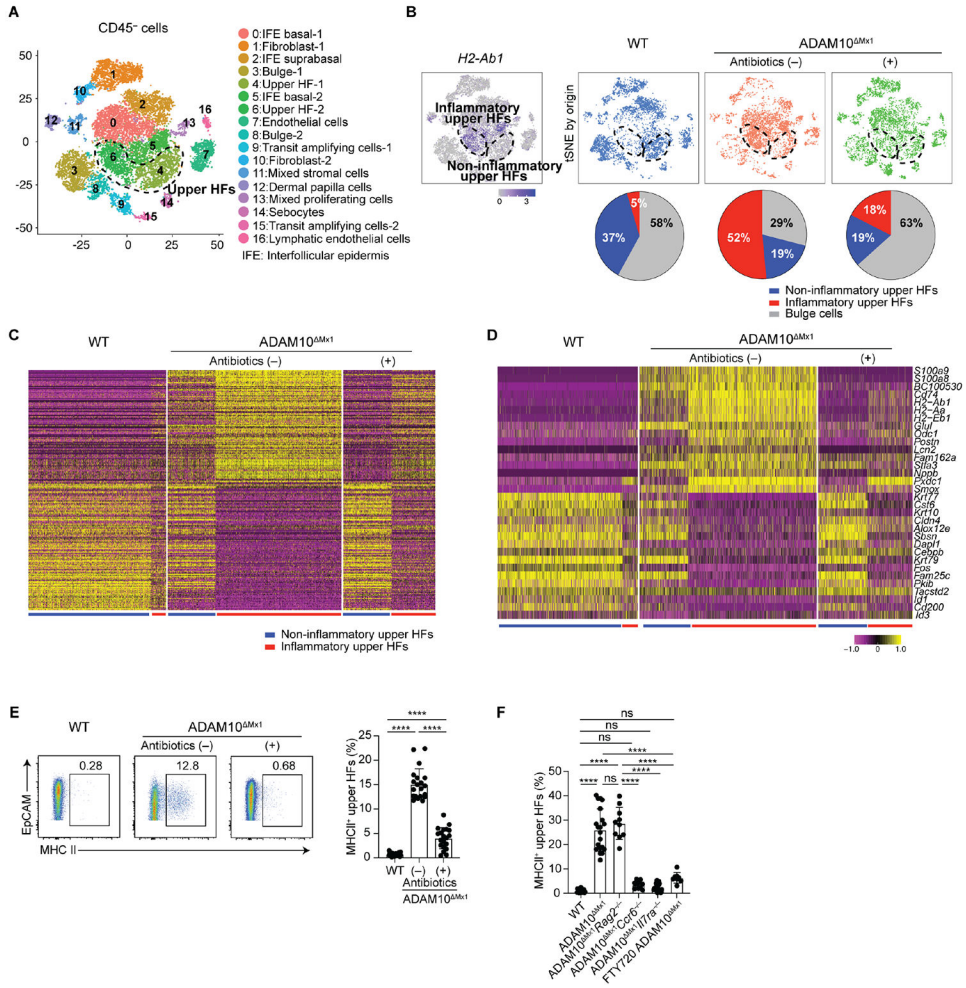

Fig. 5. Dysbiosis and inflammation underlie the immunological activation of HFs

(A) Unsupervised clustering analysis and t-SNE plot from scRNA-seq on CD45^{-} cells sorted from the skin of WT and ADAM10$^{\Delta Mx1}$ mice (antibiotic-treated and -untreated, three pooled mice from each group). (B) *H2-Ab1* expression depicting inflammatory and non-inflammatory uHF clusters. Origin-based t-SNE plots and pie charts showing HF cluster frequencies. Overview heatmap (C) and (D) those for selected genes in uHFs from indicated mice. (E) Flow cytometry for MHC II^{+} uHF cells from indicated mice and quantification (n=20 per group). (F) Quantification of MHC II^{+} uHF cells via flow cytometry from indicated mice (n=8–20 per group).

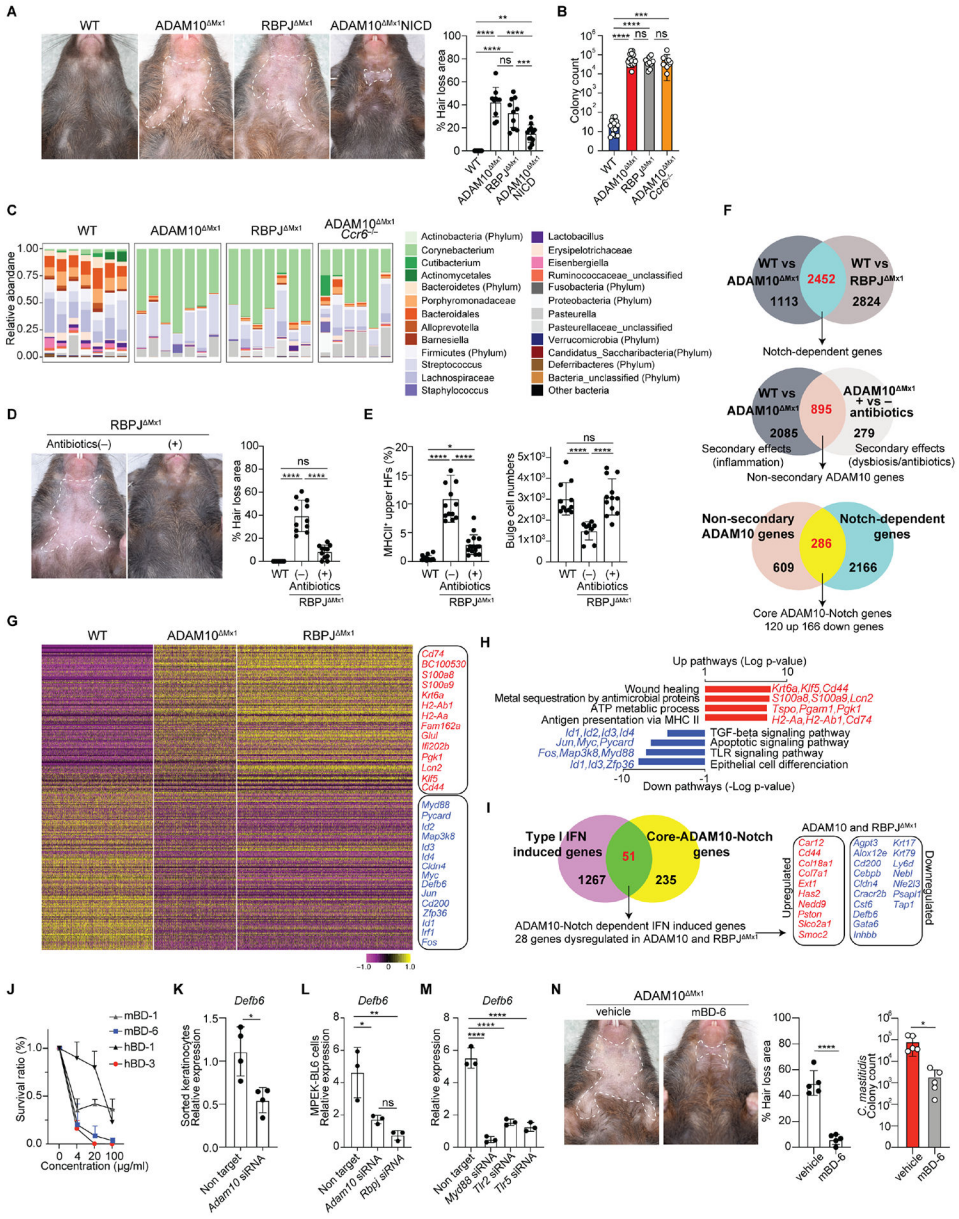

Fig. 6. ADAM10-Notch signaling axis regulates host-microbial symbiosis

(A) Gross phenotype and hair loss area in indicated mice (n=9–12). (B) Total colony counts from skin (n=9–15) and (C) 16S microbiome analysis on skin swabs from indicated mice (n=6–7). (D) Gross phenotypes and hair loss area (n=11) and (E) quantification of MHC II^{+} uHF and bulge cells from indicated mice (n=10–15). (F) scRNA-seq analysis of uHFs. Venn diagrams show the number of overlapping genes from indicated comparisons. (G) Heatmap of core 286 genes from (F) in indicated mice, annotated for selected genes and (H) pathway analysis. (I) Venn diagram showing overlapping genes from indicated comparisons and the list of dysregulated genes. Type I IFN induced genes were identified by bulk RNAseq from infundibulum of WT mice with or without poly(I:C) injection (n=4). (J) Bactericidal activity of mBD-6 and 1, hBD-1 and −3 against *C. mastitidis* (n=3, two independent experiments). *Defb6* mRNA expression after siRNA knockdown of indicated

genes in (K) sorted uHF keratinocytes and (L, M) MPEK-BL6 cells (n=3, two independent experiments). (N) Gross phenotype, hair loss area and *C. mastitidis* colony count from skin swab cultures of ADAM10$^{\Delta Mx1}$ mice treated with topical mBD-6 or vehicle (n=5, pooled from two independent experiments).

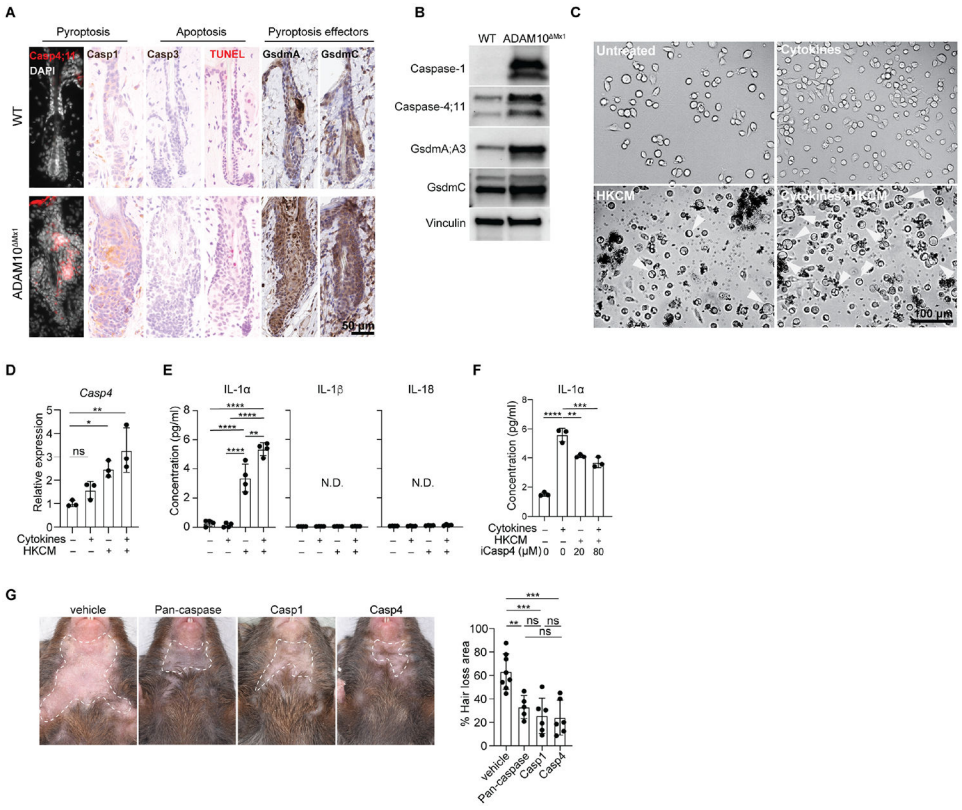

Fig. 7. Inflammatory caspases execute HF destruction

(A) Representative immunofluorescence microscopy and immunohistochemistry for indicated molecules. Casp: caspase; Gsdm: gasdermin (B) Western blot analysis for indicated molecules from isolated WT and ADAM10$^{\Delta Mx1}$ mouse keratinocytes (n=2, three mouse skin samples were for each group. Representative of two independent experiments) . (C) Morphology of MPEK-BL6 cells treated with ILC-derived cytokine cocktails, HKCM, or both. Arrowheads depict pyroptotic cells. Representative of >5 experiments. (D) Real-time PCR for *Casp4* in MPEK-BL6 cells treated with cytokine cocktail, HCKM, or both and (E) IL-1α, IL-1β, and Il-18 quantification via ELISA in culture supernatant (n=3, two independent experiments). (F) IL-1α quantification in culture supernatant of MPEK-BL6 cells treated with HKCM and caspase-4 inhibitor, Z-YVAD-FMK (n=3, two independent experiments). (G) Gross phenotype and hair loss area of indicated mice (n=5–8 per group, pooled from two independent experiments).

KEY RESOURCES TABLE

REAGENT or RESOURCE	SOURCE	IDENTIFIER
Antibodies		
Flow cytometry and MACS		
BV421 anti-mouse CD34 (RAM34)	BD Horizon	Cat# 562608; RRID: AB_11154576
BV711 anti-mouse IA-IE (M5/114.15.2)	BD Horizon	Cat# 563414; RRID: AB_2738191
AF647 anti-mouse CD31 (MEC13.3)	Biolegend	Cat# 102516; RRID: AB_2161029
APC/Cy7 anti-mouse Ly-6A/E (Sca-1) (D7)	Biolegend	Cat# 108126; RRID: AB_10645327
BUV395 anti-mouse CD45 (30-F11)	BD Horizon	Cat# 564279; RRID: AB_2651134
PE anti-mouse CD200 (OX2) (OX-90)	Biolegend	Cat# 123808; RRID: AB_2073942
PE/Cy7 anti-mouse CD326 (Ep-CAM) (G8.8)	Biolegend	Cat# 118216; RRID: AB_1236471099
AF488 anti-mouse CD117 (c-kit) (2B8)	Biolegend	Cat# 105816; RRID: AB_493472
BV421 anti-mouse CD45 (30F-11)	Biolegend	Cat# 103134; RRID: AB_2562559
APC/Cy7 anti-mouse CD45	Biolegend	Cat# 103116; RRID: AB_312981
BV650 anti-mouse CD45	Biolegend	Cat# 103151; RRID: AB_2565884
FITC anti-mouse CD2 (RM2-5)	Biolegend	Cat# 100105; RRID: AB_312652
PerCP/Cy5.5 anti-mouse CD2 (RM2-5)	Biolegend	Cat# 100116; RRID: AB_2563502
PerCP/Cy5.5 anti-mouse CD11c (N418)	Biolegend	Cat# 117328; RRID: AB_2129641
PerCP/Cy5.5 anti-mouse CD19 (6D5)	Biolegend	Cat# 115534; RRID: AB_2072925
PerCP/Cy5.5 anti-mouse CD3e (145-2C11)	Biolegend	Cat# 100328; RRID: AB_893318
PerCP/Cy5.5 anti-mouse CD11b (M1/70)	Biolegend	Cat# 101228; RRID: AB_893232
PerCP/Cy5.5 anti-mouse CD5 (53-7.3)	Biolegend	Cat# 100624; RRID: AB_2563433
PerCP/Cy5.5 anti-mouse FcεRlα (MAR-1)	Biolegend	Cat# 134320; RRID: AB_10641135
PerCP/Cy5.5 anti-mouse NK-1.1 (PK136)	Biolegend	Cat# 108728; RRID: AB_2132705
APC anti-mouse TCR γ/δ (GL3)	Biolegend	Cat# 118116; RRID: AB_1731813
BUV395 anti-mouse CD90.2 (53-2.1)	BD Horizon	Cat# 565257; RRID: AB_2739136
PE anti-mouse CCR2 (475301)	R&D	Cat# FAB5538P; RRID: AB_10718414
PE-CF594 anti-mosue CD4 (RM4-5)	BD Horizon	Cat# 562285; RRID: AB_11154410
PE/Cy7 anti-mouse CD196 (CCR6) (29-2L17)	Biolegend	Cat# 129816; RRID: AB_2072798
BV421 anti-mouse CD8 (53-6.7)	Biolegend	Cat# 100738; RRID: AB_11204079
AF647 aniti-mosue GATA3 (L50-823)	BD Pharmingen	Cat# 560068; RRID: AB_1645316
PE anti-mouse RORγt (Q31-378)	BD Pharmingen	Cat# 562607; RRID: AB_11153137
PE-eFluor 610 IL-17 A Monoclonal Antibody (eBio17B7)	eBioscience	Cat# 61-7177-82; RRID: AB_2574656
AF488 IL-13 Monoclonal Antibody (eBio13A)	eBioscience	Cat# 53-7133-82; RRID: AB_2016708
PE IL-5 Monoclonal Antibody (TRFK5)	eBioscience	Cat #12-7052-81; RRID: AB_763588
BV421 anti-mouse CD11b	Biolegend	Cat# 101236; RRID: AB_11203704
BV650 anti-mouse CD11c	Biolegend	Cat# 117339; RRID: AB_2562414
BV711 anti-mosue Ly6c	Biolegend	Cat# 128037; RRID: AB_2562630
APC/Cy7 anti-mouse CD326 (Ep-CAM)	Biolegend	Cat# 118218; RRID: AB_2098648

REAGENT or RESOURCE	SOURCE	IDENTIFIER
PE-CF594 anti-mosue CD64	Biolegend	Cat# 139320; RRID: AB_2566559
PE/Cy7 anti-mouse I-A/I-E	Biolegend	Cat# 107630; RRID: AB_2069376
AF647 anti-mouse CD45 (30-F11)	Biolegend	Cat# 103124; RRID: AB_493533
APC/Cyanine7 anti-mouse CD3ε Antibody (145-2C11)	Biolegend	Cat# 100330; RRID: AB_1877170
PE/Cyanine7 anti-mouse CD8a Antibody (53-6.7)	Biolegend	Cat# 100722; RRID: AB_312761
TruStain FcX™ (anti-mouse CD16/32) Antibody (93)	Biolegend	Cat# 101320; RRID: AB_1574975
SYTOX™ Red Dead Cell Stain, for 633 or 635 nm excitation	Thermo Fisher Scientific	Cat# S34859
CD45 MicroBeads, mouse	Milteny Biotec	Cat# 130-052-30
Purified anti-mouse CD200 (OX2)	Biolegend	Cat# 123802; RRID: AB_1236498
AF647 anti-mouse CD34 (RAM34)	BD Pharmingen	Cat# 560233; RRID: AB_1645199
Purified anti-mouse CD326 (Ep-CAM) (G8.8)	Biolegend	Cat# 118202; RRID: AB_1089027
AF488 anti-mouse CD326 (Ep-CAM) (G8.8)	Biolegend	Cat# 118210; RRID: AB_1134099
AF488 anti-mouse Ly-6A/E (Sca-1) (D7)	Biolegend	Cat# 108116; RRID: AB_493269
AF488 anti-mouse CD74 (CLIP) (In1/CD74)	Biolegend	Cat# 151006; RRID: AB_2750326
AF647 anti-mouse CD45 (30-F11)	Biolegend	Cat# 103124; RRID: AB_493533
AF647 anti-mouse/human Ki-67 (11F6)	Biolegend	Cat# 151206; RRID: AB_2566801
AF568 Goat Anti-Rat IgG H&L pre-adsorbed (polyclonal)	Abcam	Cat# ab175710; RRID: AB_2832918
AF488 rat IgG2α, κ Isotype Ctrl (RTK2758)	Biolegend	Cat# 400525; RRID: AB_2864283
Purified rat IgG2α, κ Isotype Ctrl (RTK2758)	Biolegend	Cat# 400502; RRID: AB_326523
AF488 rat IgG2α, κ isotype Ctrl (RTK4530)	Biolegend	Cat# 400625; RRID: AB_389321
AF647 rat IgG2 β, κ Isotype Ctrl (RTK4530)	Biolegend	Cat# 400626; RRID: AB_389343
Alexa Fluor™ 488 Antibody Labeling Kit	Thermo Fisher Scientific	Cat# A20181
Alexa Fluor™ 568 Antibody Labeling Kit	Thermo Fisher Scientific	Cat# A20184
ProLong™ Gold Antifade Mountant with DAPI	Thermo Fisher Scientific	Cat# P36931; RRID:
Purified caspase 1 monoclonal antibody (B0-6)	Invitrogen	Cat# MA5-32909; RRID: AB_2802544
Purified cleaved caspase 3 rabbit antibody (Asp175)	Cell Signaling Technology	Cat# 9661; RRID: AB_2341188
Purified caspase 4 monoclonal antibody (17D9)	Invitrogen	Cat# MA1-24703; RRID: AB_779521
Anti-vinculin Antibody (7F9)	Santa Cruz	Cat# sc-73614; RRID: AB_1131294
Polyclonal Rabbit anti-Human GSDMA Antibody (aa66-94)	LSBio	Cat# LS-C166692
GSDMC Polyclonal antibody	Proteintech	Cat# 27630-1-AP; RRID: AB_2880930
Peroxidase AffiniPure Goat Anti-Rabbit IgG (H+L)	Jackson Immuno Research	Cat# 111-035-003; RRID: AB_2313567
Bacterial and Virus Strains		
Corynebacterium mastitidis (CM) Isolated from mouse skin	This paper	N/A
Chemicals, Peptides, and Recombinant Proteins		
Trypsin-EDTA (0.05%)	GIBCO	Cat# 25300054
Trypsin-EDTA (0.25%)	GIBCO	Cat# 25200056
PBS, pH 7.4	GIBCO	Cat# 10010023
RPMI 1640 Medium	GIBCO	Cat# 11875-093

REAGENT or RESOURCE	SOURCE	IDENTIFIER
BenchMark™ Fetal Bovine Serum	BenchMARK™	Cat# 100-106
Antibiotic-Antimycotic (100X)	GIBCO	Cat# 15240062
Sodium Pyruvate	GIBCO	Cat# 11360070
MEM Non-Essential Amino Acids Solution	GIBCO	Cat# 15070063
Penicillin-Streptomycin (5,000 U/mL)	Thermo Fisher Scientific	Cat# 15070063
Liberase T-Flex Research Grade (500 MG)	ROCHE	Cat# 05989132001
Deoxyribonuclease I from bovine pancreas	Sigma-Aldrich	Cat# DN25-1G
beta-mercaptoethanol	GIBCO	Cat# 21985023
Leukocyte Activation Cocktail, with BD GolgiPlug™	BD Pharmingen	Cat# 550583
Zombie Aqua Fixable Viability Kit	Biolegend	Cat# 423101
FluoroFix™ Buffer	Biolegend	Cat# 422101
eBioscience™ Foxp3 / Transcription Factor Staining Buffer Set	Thermo Fisher Scientific	Cat# 00-5523-00
Opti-MEM™ I Reduced Serum Medium	GIBCO	Cat# 31985062
PCT Epidermal Keratinocyte Medium, Defined	Zenbio	Cat# CnT-07
Lipofectamine™ 2000 Transfection Reagent	Thermo Fisher Scientific	Cat# 11668019
5X siRNA Buffer	Dharmacon	Cat# B-002000-UB-100
Tween 80	Millipore sigma	Cat# P4780
BHI (Brain Heart Infusion) Broth	Hardy Diatnostics	Cat# K25
Sodium hydroxide solution	Millipore sigma	Cat# 1091371003
Hydrochloric acid	Millipore sigma	Cat# 1090601000
Phosphate buffer solution	Millipore sigma	Cat# P5244-100ML
Sodium bicarbonate	Millipore sigma	Cat# S6297
β -Defensin-1 (Human)	Peptides International	Cat# PDF-4337-s
β -Defensin-3 (Human)	Peptides International	Cat# PDF-4382-s
Recombinant Mouse Beta-defensin 6 (Defb6)	Cusabio	Cat# CSB-YP852771MO
Recombinant Mouse Beta-defensin 1 (defb1)	Cusabio	Cat# CSB-EP006662MO
Synthetic mouse bDef6 peptide	Lifeome	Cat# Mu_bDef6-10mg
SuperScript™ IV VILO™ Master Mix with ezDNase™ Enzyme	Thermo Fisher Scientific	Cat# 11766050
Fast SYBR™ Green Master Mix	Thermo Fisher Scientific	Cat# 4385612
MicroAmp™ Fast Optical 96-Well Reaction Plate with Barcode, 0.1 mL	Thermo Fisher Scientific	Cat# 4346906
RNeasy Plus Micro Kit (50)	QIAGEN	Cat# 74034
Recombinant Mouse Amphiregulin Protein	R&D Systems	Cat# 989-AR-100
Recombinant Human/Mouse/Rat BMP-2 Protein	R&D Systems	Cat# 355-BM-050
Recombinant Mouse IL-13 Protein	R&D Systems	Cat# 413-ML-050
Recombinant Mouse IL-5 Protein	R&D Systems	Cat# 405-ML-025
Recombinant Mouse IL-17A Protein	R&D Systems	Cat# 421-ML-025
Polyinosine-polycytidylic acid -TLR3 agonist	Invivogen	Cat# vac-pic
Tamoxifen	Sigma-Aldrich	Cat# T5648

REAGENT or RESOURCE	SOURCE	IDENTIFIER
RU486 (mifepristone)	Sigma-Aldrich	Cat# M8046
Pan-Caspase inhibitor - Z-VAD-FMK	Invivogen	Cat# tlrl-vad
Caspase-1 inhibitor - Ac-YVAD-cmk	Invivogen	Cat# inh-yvad
Caspase-4 Inhibitor Z-YVAD-FMK	R&D	Cat# FMK005
Fingolimod (FTY720) HCl	Shelleckchem	Cat# S5002
InVivoPlus anti-mouse Thy1.2 (CD90.2)	Bio X cell	Cat# BP0066; RRID: AB_1107682
InVivoPlus rat IgG2b isotype control, anti-keyhole limpet hemocyanin	Bio X cell	Cat# BP0090; RRID:AB_2891360
Mouse CCL20/MIP-3 alpha Antibody	R&D	Cat# MAB760; RRID: AB_2291028
Rat IgG1 Isotype Control	R&D	Cat# MAB005; RRID: AB_357348
Baytril 100 (Enrofloxacin)	Bayer	N/A
Triple antibiotic ointment	Perrigo	N/A
Cefazolin	WG Critical Care	Cat# 44567-707-25
Nonfat dry milk for western blotting applications	Bio-Rad	Cat# 170-6404
Gram's crystal violet solution	Sigma	Cat# 94448
LIVE/DEAD™ *Bac*Light™ Bacterial Viability Kit, for microscopy	Thermo Fisher Scientific	Cat# L7007
Sunflower seed oil from Helianthus annuus	Sigma-Aldrich	Cat# S5007
Dimethyl sulfoxide	Sigma-Aldrich	Cat# D2650
TRIzol™ LS Reagent	Thermo Fisher Scientific	Cat# 10296028
RIPA Buffer (10X)	Cell Signaling Technology	Cat# 9806
Protease/Phosphatase Inhibitor Cocktail (100X)	Cell Signaling Technology	Cat# 5872S
NuPAGE™ LDS Sample Buffer (4X)	Invitrogen	Cat# NP0007
NuPAGE™ Sample Reducing Agent (10X)	Invitrogen	Cat# NP0009
Trans-Blot Turbo RTA Midi 0.45 µm LF PVDF Transfer Kit	Bio-Rad	Cat# 1704275
4–20% Criterion™ TGX™ Precast Midi Protein Gel, 18 well	Bio-Rad	Cat# 5671094
Trans-Blot® Turbo™ Transfer System	Bio-Rad	Cat# 1704150
ChemiDoc Touch Systems	Bio-Rad	Cat# 1708370
Pierce™ 20X TBS Tween™ 20 Buffe	Thermo Fisher Scientific	Cat# 28360
Pierce™ ECL Western Blotting Substrate	Thermo Fisher Scientific	Cat# 32106
Critical Commercial Assays		
Mouse IL-1α ELISA Kit	Abcam	Cat# ab199076
Mouse IL-1β ELISA Kit	Abcam	Cat# ab197742
Mouse IL-18 ELISA Kit	Abcam	Cat# ab216165
Mouse MIP3 alpha ELISA Kit (CCL20)	Abcam	Cat# ab100728
Deposited Data		
Transcriptomic profiles of type I/III interferon-responsive hair follicle subsets from WT with or without Poly:IC injection	This paper	GEO: GSE180435
Transcriptomic profiles of type I/III interferon-responsive hair follicle subsets from ROSA26YFP_Mx1 and ADAM10;ROSA26YFP_Mx1 mice	This paper	GEO: GSE180798

REAGENT or RESOURCE	SOURCE	IDENTIFIER
Single-cell transcriptomic profiles of CD45-negative cells from WT (C57BL/6), antibiotics non-treated Mx1Cre-Adam10f/f and antibiotics treated Mx1Cre-Adam10f/f mice	This paper	GEO: GSE180723
Single-cell transcriptomic profiles of CD45-positive cells from Mx1-Cre x Adam10f/f Rag2KO mice	This paper	GEO: GSE180405
Single-cell transcriptomic profiles of CD45-negative cells from Mx1Cre-Rbpjf/f mice	This paper	GEO: GSE180718
Microbiome	This paper	BioProject: PRJNA749624
Experimental Models: Cell Lines		
Epidermal Keratinocyte Progenitors, Mouse BL6	Zen-Bio	Cat# MPEK-BL6
Experimental Models: Organisms/Strains		
Mouse: C57BL/6J	The Jackson Laboratory	Jax: 000664
Mouse: B6.129X1-Gt (ROSA)26Sor$^{tm1(EYFP)Cos}$/J (ROSA-EYFP)	The Jackson Laboratory	Jax: 006148
Mouse: B6.Cg-Tg(Mx1-cre)1Cgn/J	The Jackson Laboratory	Jax: 003556
Mouse: Adam10tm1.1Khr (Adam10-floxed)	Yoda et al., 2011	N/A
Mouse: B6.129P2-Ccr6^{tm1Dgen}/J	The Jackson Laboratory	Jax: 005793
Mouse: B6.129S4-Ccr2^{tm1Ifc}/J	The Jackson Laboratory	Jax: 004999
Mouse: B6(Cg)-Rag2$^{tm1.1Cgn}$/J	The Jackson Laboratory	Jax: 008449
Mouse: B6.129S7-Il7r^{tm1Imx}/J	The Jackson Laboratory	Jax: 002295
Mouse: C57BL/6NTac.Cg-*Rag2^{tm1Fwa} Il2rg^{tm1Wjl}*	Taconic Biosciences	Taconic: 4111-F
Mouse: Rbpj^{tm1Hon}	Han et al., 2002	N/A
Mouse: Gt(ROSA)26Sor$^{tm1(Notch1)Dam}$/J	The Jackson Laboratory	Jax: 008159
Mouse: Lrig1$^{tm1.1(cre/ERT2)Rjc}$/J	The Jackson Laboratory	Jax: 018418
Mouse: B6;SJL-Tg(Krt1-15-cre/PGR)22Cot/J	The Jackson Laboratory	Jax: 005249
Mouse: C57BL/6-Tg(Csf1r-cre)1Mnz/J	The Jackson Laboratory	Jax: 029206
Oligonucleotides		
ON-TARGETplus Non-targeting Control Pool	Dharmacon	Cat# D-001810-10-20
ON-TARGETplus Mouse Adam10 siRNA, SMARTPool	Dharmacon	Cat# L-041092-00-0020
ON-TARGETplus Mouse Rbpj siRNA, SMARTPool	Dharmacon	Cat# L-042742-01-0020
ON-TARGETplus Mouse Tlr5 siRNA, SMARTPool	Dharmacon	Cat# L-049160-01-0020
ON-TARGETplus Mouse Tlr2 siRNA, SMARTPool	Dharmacon	Cat# L-062838-02-0020
ON-TARGETplus Mouse Myd88 siRNA, SMARTPool	Dharmacon	Cat# L-063057-00-0020
PrimePCR™ PreAmp for SYBR® Green Assay: Adam10, Mouse	Bio-Rad	N/A
PrimePCR™ PreAmp for SYBR® Green Assay: Rbpj, Mouse	Bio-Rad	N/A
PrimePCR™ PreAmp for SYBR® Green Assay: Defb6, Mouse	Bio-Rad	N/A
PrimePCR™ PreAmp for SYBR® Green Assay: Tlr5, Mouse	Bio-Rad	N/A
PrimePCR™ PreAmp for SYBR® Green Assay: Tlr2, Mouse	Bio-Rad	N/A
PrimePCR™ PreAmp for SYBR® Green Assay: Myd88, Mouse	Bio-Rad	N/A

REAGENT or RESOURCE	SOURCE	IDENTIFIER
PrimePCR™ PreAmp for SYBR® Green Assay: Casp1, Mouse	Bio-Rad	N/A
PrimePCR™ PreAmp for SYBR® Green Assay: Casp4, Mouse	Bio-Rad	N/A
Primer Rplp0 Forward: TGGTCATCCAGCAGGTGTTCGA Reverse: ACAGACACTGGCAACATTGCGG	Eurofin	N/A
Recombinant DNA		
None		
Software and Algorithms		
FlowJo	FlowJo, LLC	https://www.flowjo.com/solutions/flowjo
GraphPad Prism	GraphPad Software	https://www.graphpad.com/
Seurat	Satija Lab	https://satijalab.org/seurat/
ImageJ	National Institutes of Health	https://imagej.nih.gov/ij/
Other		
Corning® BioCoat™ Collagen I 24-well Clear Flat Bottom TC-treated Multiwell Plate, with Lid	Corning	Cat# 356408
Corning® BioCoat™ Collagen I 48-well Clear Flat Bottom TC-treated Multiwell Plate, with Lid	Corning	Cat# 354505
Corning® 96-well Clear Round Bottom TC-treated Microplate, Individually Wrapped, with Lid, Sterile	Corning	Cat# 3799
Blood Agar (TSA with 5% Sheep Blood), 85mm Monoplate	Thermo Fisher Scientific	Cat# R01202
BHI (Brain Heart Infusion) Broth, 10ml, 16x125mm tube	Hardy Diagnostics	Cat# K25
BHI (Brain Heart Infusion) Agar, deep fill, 15x100mm plate	Hardy Diagnostics	Cat# W15
Falcon® 40 μm Cell Strainer, Blue, Sterile, Individually Packaged, 50/Case	Corning	Cat# 352340
Falcon® 100 μm Cell Strainer, Yellow, Sterile, Individually Packaged, 50/Case	Corning	Cat# 352360
Tungsten Carbide Beads, 3 mm	Qiagen	Cat# 69997
Direct-zol RNA Microprep Kits	Zymo reserch	Cat# R2062
NEBNext® Poly(A) mRNA Magnetic Isolation Module	New England BioLabs	Cat# E7490S
NEBNext® Ultra RNA Library Prep Kit for Illumina	New England BioLabs	Cat# E7530S
NEBNext® Multiplex Oligos for Illumina (Index Primers Set 1)	New England BioLabs	Cat# E7335S
NEBNext® Multiplex Oligos for Illumina (Index Primers Set 2)	New England BioLabs	Cat# E7500S